Fluorescent nuclear track detectors – Review of past, present and future of the technology

Akselrod, Mark; Kouwenberg, Jasper

Important note
To cite this publication, please use the final published version (if applicable).
Please check the document version above.

Fluorescent Nuclear Track Detectors –

review of past, present and future of the technology

Mark Akselrod[a] and Jasper Kouwenberg[b]

[a] *Landauer, Crystal Growth Division, Stillwater, OK, USA*

[b]*Delft Technical University, Delft, the Netherlands*

1.   ABSTRACT

Fluorescent Nuclear Track Detector technology is a passive luminescent integrating detector technology having important advantages in measuring neutrons, heavy ions and even photons. FNTD is based on new aluminum oxide crystals doped with carbon and magnesium impurities (Al_2O_3:C,Mg) and confocal laser scanning fluorescent microscopy technique. The production and optical characteristics of Mg-doped aluminum oxide are discussed in details, as well as the progress made in the read-out instrumentation. Since the introduction of the technology, FNTDs have been successfully used for a wide range of applications in mixed neutron-gamma fields, medical dosimetry and radiobiological research and the results of these tests are discussed in detail.

2.   INTRODUCTION

Neutron and heavy charged particle dosimetry is considered the most difficult task in radiation dosimetry. Neutrons may have a wide dynamic range of energies and doses and are not directly ionizing. Heavy charged particles also might have a very wide range of linear energy transfer (LET) and penetration range in matter. Active neutron instruments like [3]He-based counters, Rem-meters and Bonner Sphere spectrometers are typically bulky, require long preparation, calibration and readout time and are prone to failure because of batteries and complex electronics. Conversely, passive integrating detectors like TLD and OSLD are very compact, reusable and reliable, as they do not have batteries or imbedded electronics. They do not require much preparation and post processing, although they do not have the alarming and dose rate indication capabilities.

2.1. Neutron Detectors

For many years the most popular types of passive neutron detectors were albedo TLDs based on pairs of ^{6}LiF/^{7}LiF (Piesch and Burgkhardt, 1985) , plastic nuclear track detectors (PNTDs) (Cassou and Benton, 1978) and superheated emulsion or bubble detectors (d'Errico, 2001). Each of these technologies has its own technical and practical advantages and disadvantages.

Albedo TLDs take advantage of the high neutron capture cross-section of ^{6}Li and are very sensitive to thermal and epithermal neutrons and can use standard automatic TLD readers. In the case of fast neutrons, albedo TLDs rely on thermalization of fast neutrons by the human body and complex filtering/shielding configuration of the badge that involves several Cd or ^{10}B filters absorbing thermal neutrons to discriminate between incident thermal and albedo neutrons. Sensitivity to gamma photons as well as a strong neutron energy dependence is the problem. The albedo effect is also dependent on the person's body size and on the separation between the badge and the body resulting in poor metrological performance in mixed and unknown neutron fields.

Bubble detectors measure neutrons by forming and counting small bubbles in superheated organic fluid. They demonstrate good performance in different research applications due to their high neutron sensitivity and are relatively insensitive to photons, but are bulky and require temperature compensation. Instead of manually counting bubbles, automatic detection of neutron-induced bubbles can be done by acoustic pop-up detection or optical scattering.

PNTDs, like CR-39, are widely used by commercial dosimetry services as they are relatively inexpensive and allow for reliable automation of microscope image acquisition and processing. Cellulose nitrate (CN), polycarbonate (Lexan) and polyallyl diglycol carbonate (CR-39) are among just a few etchable detector materials used in neutron dosimetry. Their main advantages are insensitivity to photons, low limit of detection, wide range of detectable neutron energies and speed of readout. Major drawbacks are the need for chemical etching in concentrated NaOH, long etching time, variation in plastic material quality, limited upper dose range due to overlapping of tracks at high doses and insensitivity to high energy neutrons due to the limited LET range above 5 keV/µm of detectable recoil protons.

2.2. (Heavy) ion detectors

Detection methods for (heavy) ions partly overlap with techniques for neutron detection, but are generally easier to measure due to the directly ionizing properties of these particles. Ionization chamber dosimetry is often considered the

primary standard for (clinical) ion dosimetry, while special attention should be payed to the calibration of the relatively high recombination correction factor in high LET ion beams for these types of detectors (Boutillon, 1998; Kanai, 1998). TLD and OSLD are proven technologies that can be used for ion dosimetry. However, research has shown that charge and energy resolution for these types of detectors are relatively poor, therefore requiring extensive calibration of the response curves in order to accurately estimate the biological dose (Karger, 2010).

The use of PNTDs and semiconductor detectors is widespread for ion spectroscopy. Similar to their use in neutron dosimetry, can the size and depth of the holes after etching be used to deduct the energy and charge of incident ions. Drawbacks of this detector for ion radiation are similar to those described for neutron radiation. Semiconductor detectors offer online read-out and a better energy and charge resolution, but do require large arrays of small volume detectors in order to extract 3D track information, reducing signal-to-noise ratios and leading to higher costs due to their complexity. Calibration with ionization chambers is usually required for absolute dosimetry with semiconductor detectors (Bradley, 2001).

The detection of alpha radiation offers additional challenges compared to clinical ion beams due to the very short range in matter for these particles. The maximum range of 100 μm in water makes it that these particles are unable to penetrate most walled radiation measurement devices. OSLD (Oster et al., 2010), radiochromic film (Aydarous and Ghazaly, 2013), ionization chambers, PNTD (Wertheim et al., 2010), semiconductor detectors (Chaudhuri et al., 2013; Wang et al., 2012) and more recently the alpha camera, consisting of a CCD camera behind a scintillator, are often applied for this type of radiation (Back and Jacobsson, 2010). The most accurate dose rate measurements are reached with the so-called extrapolation chamber with a very thin entrance window since it is able to determine the recombination correction factor in addition to the apparent dose rate (Böhm et al., 1991).

While this does not yet cover all available radiation detection, dosimetry and spectroscopy methods, it can be concluded that a need for passive detectors for (clinical) ion beams with good energy and charge resolution still exists.

2.3.   Fluorescent Nuclear Track Detector

Novel passive integrating fluorescent nuclear track detectors (FNTDs), developed by Landauer, Inc. (Akselrod and Akselrod, 2006; G. M. Akselrod et al., 2006; Sykora et al., 2007, 2008a, 2009) have demonstrated a promising performance for dosimetry of neutrons, protons and other heavy charged particles. The FNTD is based on a single crystal of aluminum oxide doped with carbon and magnesium, and having aggregate oxygen vacancy defects - Al_2O_3:C,Mg

(Akselrod et al., 2003; Sanyal and Akselrod, 2005). The crystals are grown by the Czochralski technique, and detectors are produced in different sizes and shapes depending on the final application (Figure 1). Thin 500 μm polished wafers with diameter as large as 60 mm for radiation field imaging can be produced. The tracks of recoil protons and other heavy charged particles, or even delta electrons, generated in a crystalline detector which appear as bright objects on a dark background in fluorescent contrast, are imaged digitally and processed using a high resolution readout system based on the confocal laser scanning fluorescence microscopy technique (Akselrod et al., 2014a; Diaspro, 2001; Sykora et al., 2008b). Specialized data acquisition and image processing software allows for automatic readout of multiple detectors in two modes: track counting in a low dose range and analog, power spectral integral (PSI) mode for high doses. This article is a review of the advancements of FNTD technology during the last decade. We cover the fundamentals of FNTD crystals' defects, optical properties and production, the readout process and advances in both fast and super-resolution readout, the application in neutron spectroscopy and dosimetry, gamma dosimetry, LET spectroscopy of ions and radiobiological research.
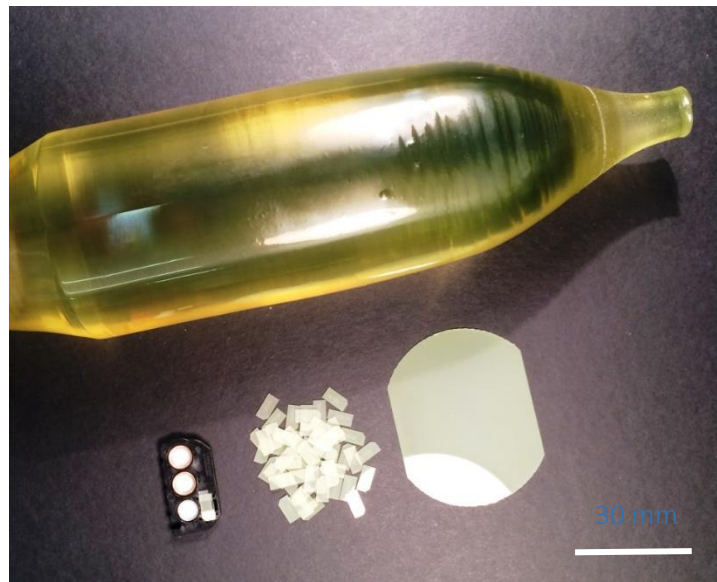

Figure 1: Al_2O_3:C,Mg single crystal (top), polished wafer (bottom right), FNTDs (bottom middle) and OSL slide with FNTD chip covered by three converters (polyethylene, PTFE and Li-glass) (bottom left).

3. CRYSTAL GROWTH, DEFECTS AND OPTICAL SPECTROSCOPY OF ALUMINUM OXIDE CRYSTALS

3.1. *Crystal growth*

Al_2O_3:C,Mg crystals are synthesized using the Czochralski (CZ) crystal growth method (Akselrod and Bruni, 2012), the technique of pulling the crystal out of a melt by first dipping in a seed of the same material of desired crystallographic orientation in the melt with simultaneous seed rotation. Today the Czochralski technique is the major industrial growth method for virtually all semiconductor materials that melt congruently as well as a variety of oxide crystals. Sapphire with desired impurities is melted above the crystallization point of 2050 °C in a highly reduced atmosphere (Figure 2).

Oxygen vacancy defects are introduced by growing the crystal in the presence of hot graphite to obtain a low partial oxygen pressure around 10^{-20} Pa. By dissolving carbon monoxide at a preferred concentration during crystal growth into the melt, carbon dopants are formed during the crystallization. It is believed that secondary effects of the presence of carbon monoxide during crystal growth involve the creation of oxygen vacancies. Magnesium is added in the form of a Mg-compound, often MgO or $MgAl_2O_4$, to the raw material.

FNTDs are cut from the Al_2O_3:C,Mg crystal along the optical *c*-axis in different shapes, although commonly found as 8 x 4 x 0.5 mm^3 plates (Figure 1). One large side of the detector is polished to optical quality. To reduce background luminescence, detectors are thermally annealed with a special heating profile up to 650 °C for 17 hours and optically bleached with a frequency tripled 349 nm Nd:YLF pulsed laser light. Annealing or optical bleaching can be repeated to erase fluorescent tracks in a detector, allowing it to be reused.
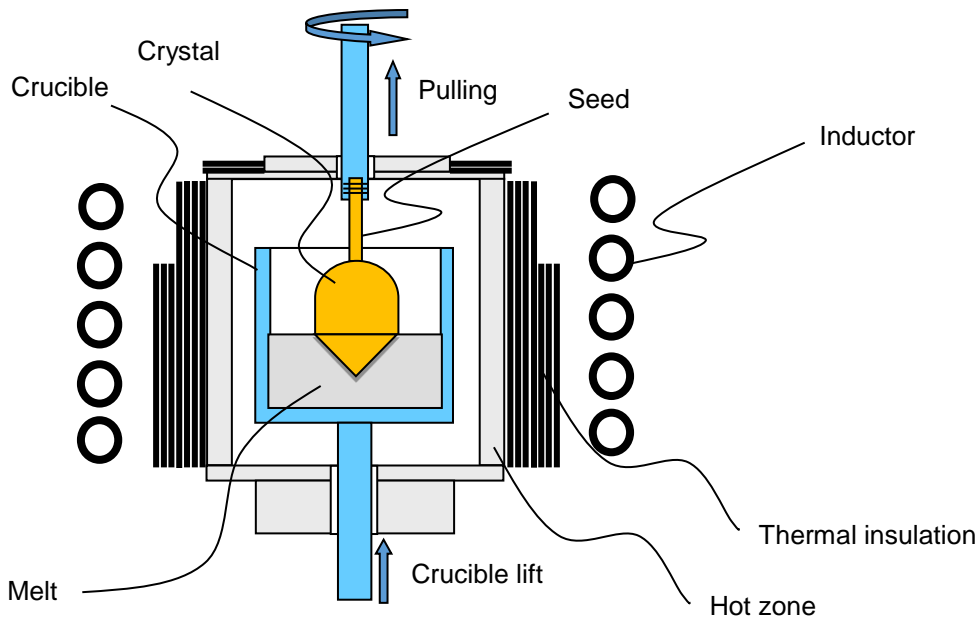
Figure 2: Schematic diagram of the Czochralski crystal growth process (Akselrod and Bruni, 2012).

3.2.   Crystallography, defect structure and spectroscopy

α-Al_2O_3 has a rigid, slightly distorted hexagonal close-packed sub-lattice of O^{2-} ions with Al^{3+} ions occupying two out of every three octahedral interstices (Figure 3). Each O^{2-} ion is surrounded by four tetrahedral nearest-neighbor Al^{3+} ions. Point defects in the crystal (vacancies, interstitials and impurities) in certain circumstances can produce optically active defects known as color centers or luminescent centers. Ionized electrons produced in the crystal by radiation can be captured by said color centers, thereby altering their net charge and consequently their optical properties (Akselrod et al., 1998). A fundamental advantage of Al_2O_3 is its wide optical energy gap of 9.5 eV that allows one to engineer deep localized electronic states, traps and luminescent centers with the high thermal and optical stability required for radiation detection applications.

Crystal growth in a highly reducing atmosphere stimulates the creation of single oxygen vacancies occupied by two electrons usually denoted as F-centers. They are identified by strong optical absorption band at 205 nm and emission band at 420 nm with 35 ms lifetime (Lee and Crawford, 1979). Other two absorption bands at 230 and 255 nm with emission at 330 nm and very short lifetime of ~2 ns are assigned to transitions in single oxygen vacancies with just one electron and denoted as F^+-centers (Akselrod et al., 1990; Evans and Stapelbroek, 1978). F and F^+-centers have been studied in detail and play a key role in the TL and OSL mechanisms of Al_2O_3:C (Akselrod et al., 1990, 1998; Yukihara et al., 2015).
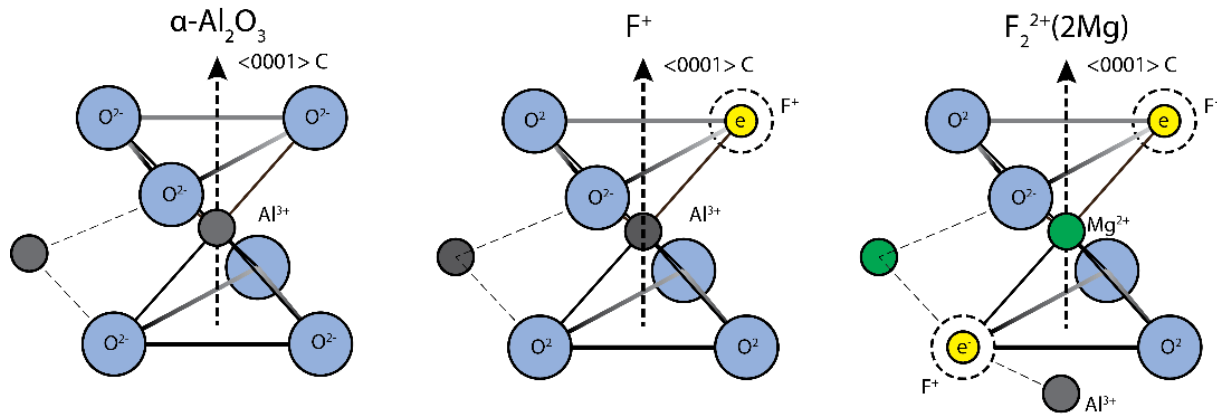
Figure 3: Lattice structure of α- Al_2O_3:C,Mg and its important defects: a) simplified ideal lattice cell, b) single oxygen vacancy with one electron – F^+ center and c) aggregate defect consistent of two oxygen vacancies charge compensated by two Mg^{2+}-ions.

Al_2O_3:C,Mg crystals have much more complex defects created during the crystal growth process that result in multiple types of color centers with different absorption and emission bands. In addition to single vacancy defects (F and F^+-centers) which dominate in Al_2O_3:C crystals, double vacancy defects (denoted as F_2-type color centers) associated with Mg-impurity ions (Figure 3c) are present. They were identified and assigned to different emission-excitation and absorption bands (Figs. 4, 5 and 6). The crystals have yellow-green coloration due to a 435 nm absorption band associated with aggregate F_2^{2+}(2Mg) color centers consisting of two oxygen vacancies charge-compensated by two magnesium ions (Figure 3c) (Akselrod et al., 2003). F_2^{2+}(2Mg) centers efficiently capture free electrons during irradiation and undergo photochromic (Figure 4) and radiochromic (Figure 5) transformations into a three-electron state forming F_2^+(2Mg) centers (G. M. Akselrod et al., 2006; Sykora and Akselrod, 2010a). The F_2^+(2Mg) centers have excitation bands centered at 335 and 620 nm with emission centered at 750 nm (Figure 6, Figure 7). Similar types of defects produced by thermo-chemical reduction of Mg-doped sapphire crystals were reported by Ramirez *et al*. (Ramirez et al., 2005).
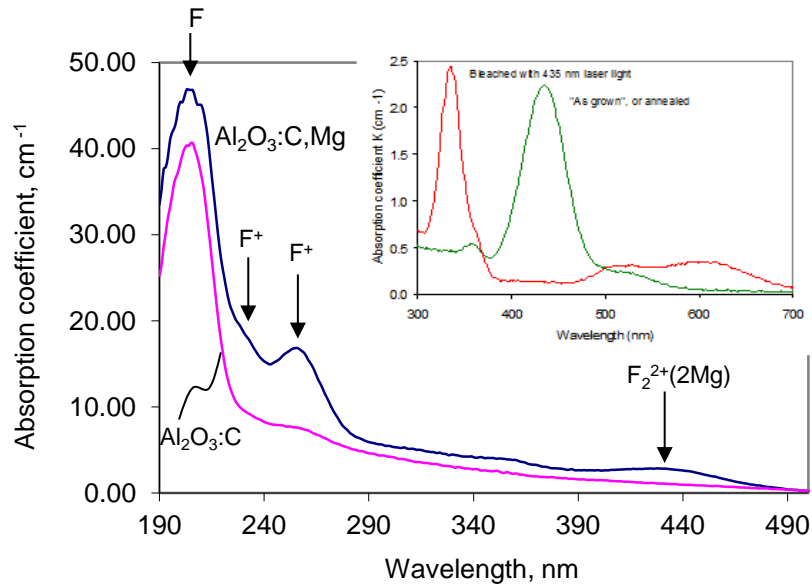
Figure 4: Optical absorption bands in Al₂O₃:C and Al₂O₃:C,Mg crystals and photochromic transformation of the latter under 435 nm pulsed laser light (Akselrod et al., 2003).
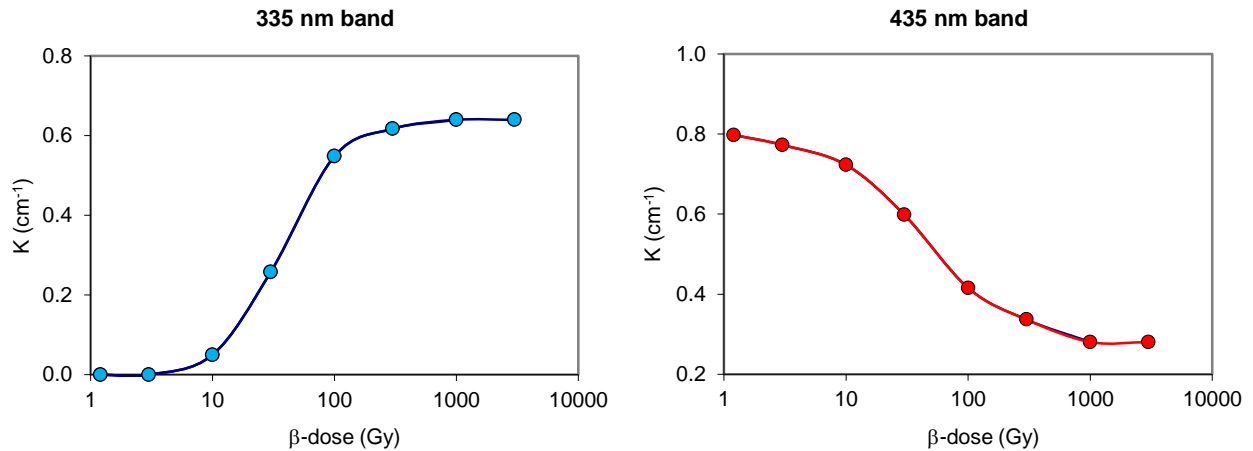

Figure 5: Radiochromic transformation of absorption bands in Al₂O₃:C,Mg crystal as a function of β-dose (G. M. Akselrod et al., 2006).

Figure 6: Photoluminescence bands in Al₂O₃:C,Mg crystals (a) before and (b) after irradiation with 143 Gy from a ⁹⁰Sr/⁹⁰Y beta source (Akselrod and Sykora, 2011).

Figure 7: Excitation and emission spectra of F₂⁺ (2Mg)-centers (Sanyal and Akselrod, 2005).

The most important advantage of this new crystal for practical applications is that the color centers undergo efficient radiochromic transformations as a function of dose (Figure 5). Functioning as charge storage, these color centers are thermally stable up to 600° C (Figure 8). The lifetime of their luminescence is short, ~ 9 ns, for an F_2^{2+}(2Mg) center emitting at 520 nm and 75 ns for an F_2^+(2Mg) center emitting at 750 nm (Figure 9) which allows for fast laser scanning in imaging applications. That lifetime is almost a million times faster than the 35 ms lifetime of F-center luminescence in OSL material based on Al_2O_3:C crystals.
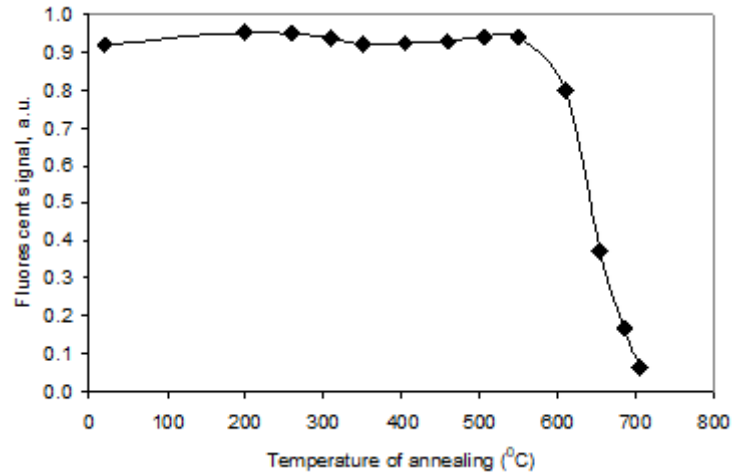

Figure 8: Thermal stability and erasure of fluorescent signal produced by F_2^+ (2Mg)-centers by thermal annealing of Al_2O_3:C,Mg crystal (G. M. Akselrod et al., 2006).
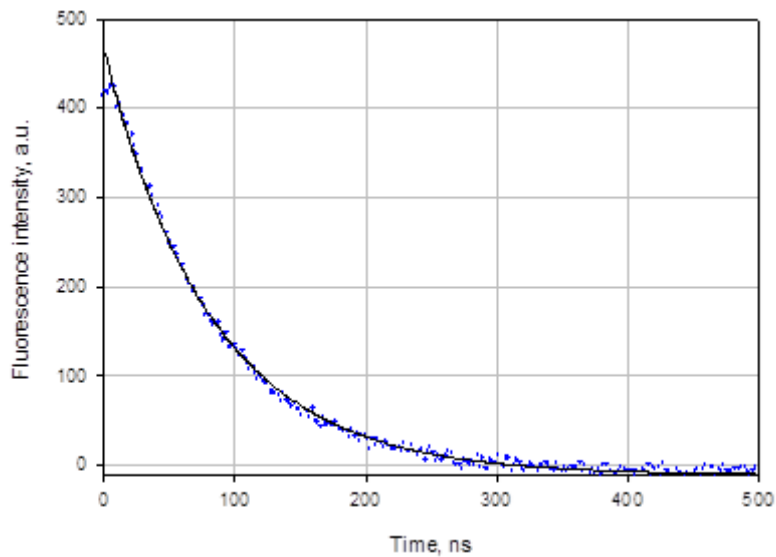

Figure 9: Fluorescence decay of F_2^+ (2Mg)-centers emission band at 750 nm having 75 ns lifetime (Akselrod et al., 2003).

Double vacancy defects which are the main luminescent centers used in FNTD technology are optically stable and can be interrogated multiple times without photoionization which provides a non-destructive readout using intra-center fluorescence. If this intra-center fluorescence is radiation-induced it is often called radio-photo-luminescence (RPL), the process explained schematically using the band diagram in Figure 10. This is in contrast with the OSL process, including the one in Al_2O_3:C, where the photoionization of traps during optical stimulation is followed by the recombination of charge on luminescent centers and results in partially destructive readout. Both physical processes - intra-center fluorescence and recombination luminescence - during OSL readout have their own practical advantages and disadvantages. The main advantage of OSL is the possibility to use inexpensive powdered phosphors imbedded in plastic to detect very low doses (~1 µSv) by measuring single photons of radiation-induced luminescence above very low background signal. Another advantage of OSL is easy bleaching/erasing of detectors for reusable applications. At the same time OSL detectors are partially erased during readout and are sensitive to ambient light requiring light-tight packaging and handling in low or even red light conditions. Conversely, RPL materials are typically not sensitive to ambient light, can be read multiple times without erasure, but show relatively high background signal even before irradiation and cannot measure very low doses. Plus, their optical erasure is more technically challenging, but possible
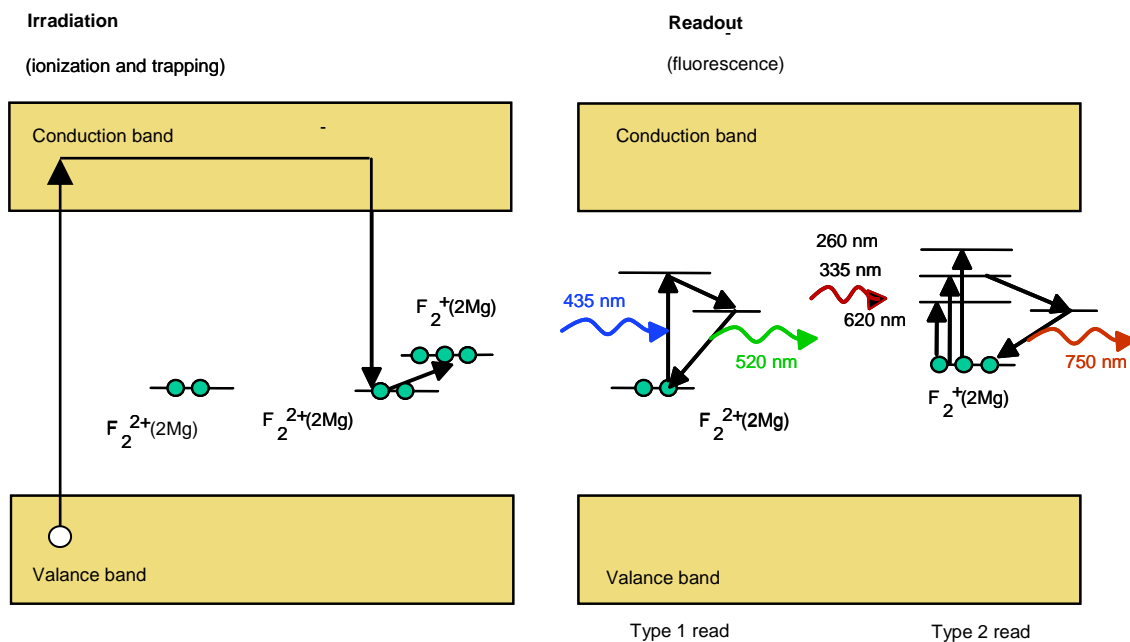
using a multiphoton ionization process. Thermal erasure of RPL phosphors is also possible.

Figure 10: Schematic band diagram of defect levels in Al$_2$O$_3$:C,Mg crystals explaining electronic processes during irradiation and optical readout using radio-photo-luminescent process (Akselrod et al., 2003).

4. ADVANCES IN FNTD INSTRUMENTATION

Due to the short relaxation time of F$_2^+$(2Mg)-centers, FNTDs can be readout using fast confocal laser scanning fluorescence measurement systems (Akselrod and Sykora, 2011). Confocal laser scanning microscopy (CLSM) is used to readout FNTDs and offers a high spatial resolution, reaching near-diffraction limit at 240×240×940 nm^3 measured as FWHM (Kouwenberg et al., 2016). The confocal microscopy technique allows one to discriminate the fluorescence induced in a tight focal laser spot within the track volume from the background fluorescence induced by the laser beam in the surrounding crystal volume. Figure 11 shows an example of a fluorescent image (2D x-y scan) where the bright spots are produced by recoil protons generated by Am-Be neutrons in a polyethylene converter mounted on top of an FNTD crystal during the irradiation. A scan is typically performed by an FNTD reader system at 1-2 µm depth in the single crystal sapphire detector. The bright fluorescent features are actually a cross-section of the track within the confocal thickness of the scanned layer. In dosimetry applications the dose of neutrons is proportional to the track density determined from statistically significant track counts obtained from multiple images of a large detector area and processed by a specialized image processing routine.
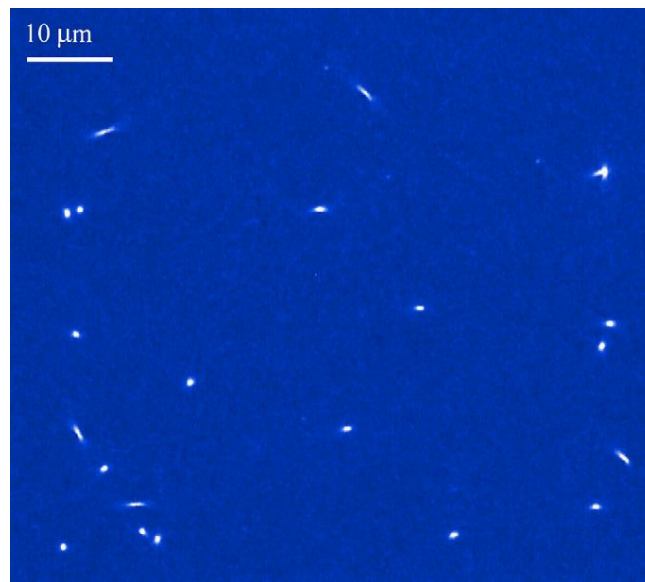

Figure 11: Example of a fluorescent 2D image of recoil proton tracks induced by fast neutrons and obtained by scanning the laser beam at 2 µm depth in a single crystal sapphire detector covered by a polyethylene converter. The

fluorescent track spots are a cross-section of the tracks within the thickness of the scanned layer (Sykora et al., 2008b).

A simplified optical diagram of a CLSM is shown in Figure 12. Light from a 635nm laser diode is scanned by a 1D or 2D galvanometer system and focused to a small volume in the crystal by a high NA objective lens. The resulting fluorescence emission is collected by the same objective (epi-luminescent mode), passed through the same optics and galvanometers (descanning), separated from the excitation laser light by a dichroic mirror and focused through a pinhole and long-pass filters onto an avalanche photodiode (APD) detector. A pinhole placed in front of the APD photodetector filters out-of-focus fluorescence for optimal spatial resolution and reduced background fluorescent signal. The CLSM creates 2D images formed by fluorescence intensity as a function of the laser beam position in an FNTD by raster scanning of the focused laser beam inside the crystal and digitizing the fluorescent signal voxel by voxel.
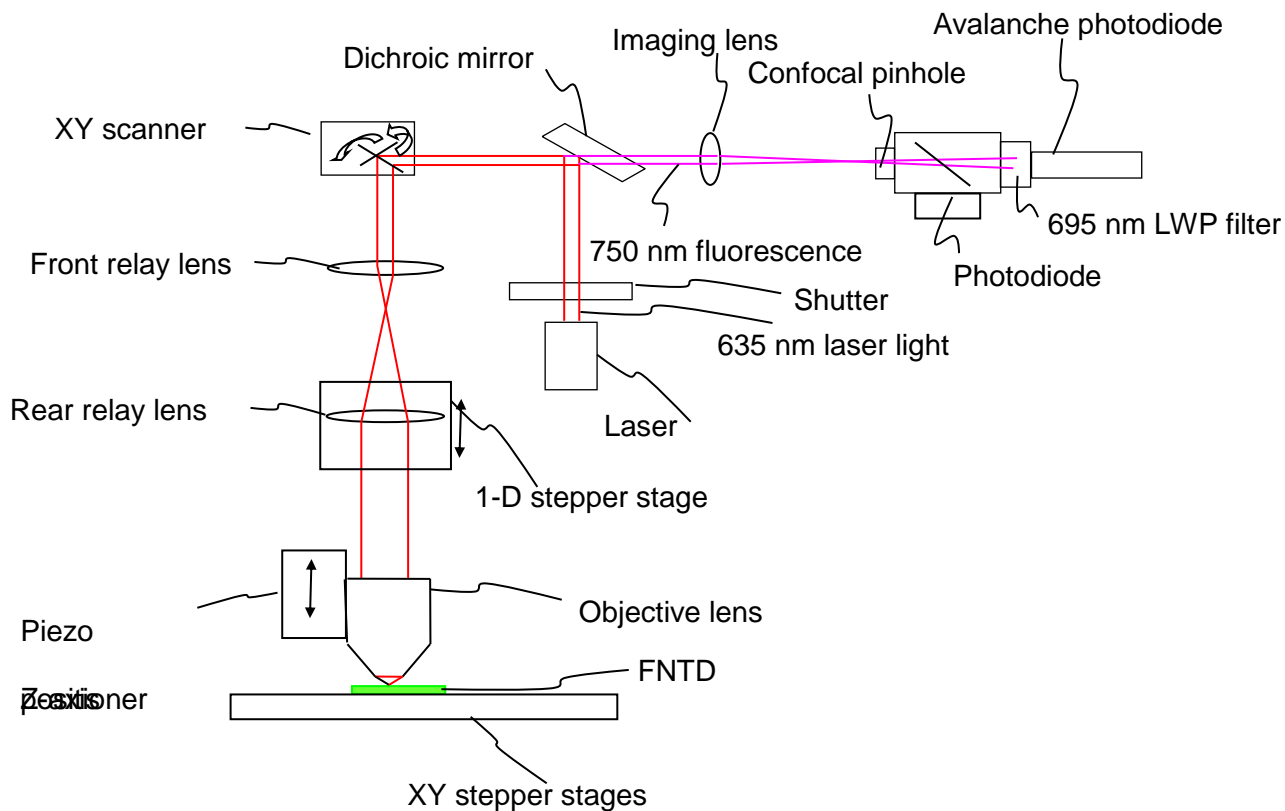

Figure 12: Simplified schematic of a CLSM used for FNTD read-out (Sykora et al., 2008b).

3D images are created by recording series of 2D images at various pre-set depths in the crystal. A 3D volumetric image can be then reconstructed from the stack of 2D images by any commercial or free software packages (Figure 13). CLSMs from a number of manufacturers (Leica, Zeiss, Olympus) can be used for FNTD read-out when outfitted with the

appropriate lasers, photodetectors and filters for the mentioned excitation and emission wavelengths. APDs are, however, a better choice since conventional photomultiplier tubes have insufficient detection efficiency at wavelengths >650 nm.
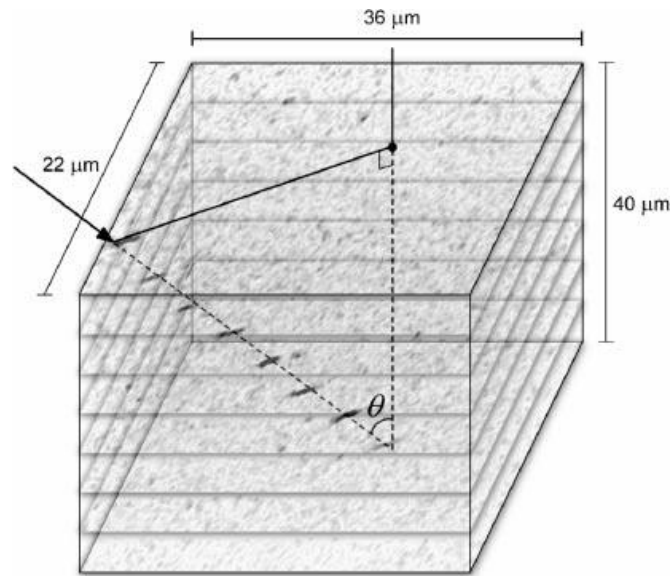

Figure 13: Stack of 2D images obtained at different depths in the crystal with the trajectory obtained by interconnecting and measuring the centroid of each fluorescent bright spot (here in negative contrast) identified on each image (G. M. Akselrod et al., 2006).

An example of a typical CLSM image of recoil protons traversing an FNTD is shown in Figure 11. Each bright spot was produced by a single proton passing through the detector. Note that the shape and intensity of the spots varies as a result of the proton's angle of incidence and the asymmetric shape of the excitation laser focal spot of the CLSM system which resembles an ellipsoid having a longer axis in the direction along the optical axis of the objective lens (Figure 14). Image and track processing and analyses are described in more details in section 5 *"Application of FNTD in radiation dosimetry"*.
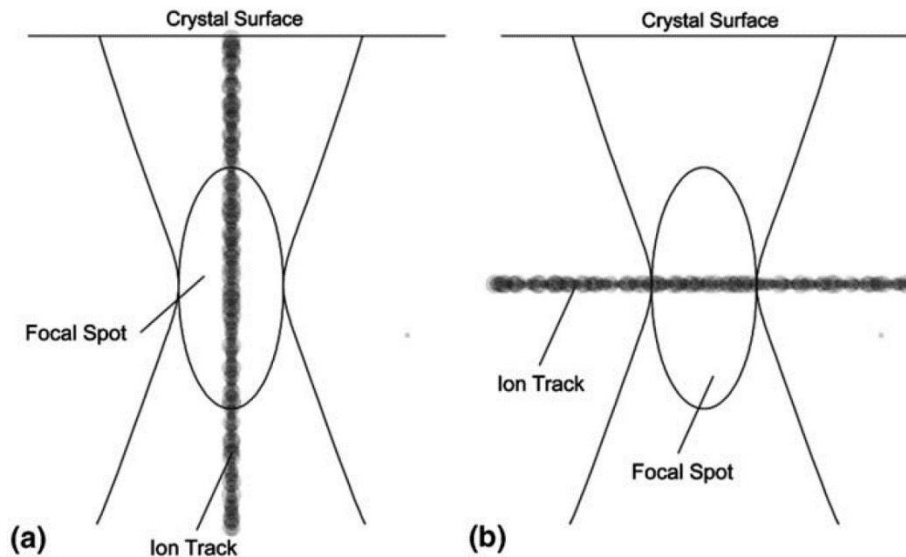
Figure 14: Illustration of the effect of the focal spots asymmetry on the illumination of ion tracks at different angles (M. S. Akselrod et al., 2006). *The convex lines indicate the excitation laser beam, where the maximum intensity in the focal spots is visualized as an ellipse. A track perpendicular to the crystal surface will produce a near 3-times higher fluorescence intensity than tracks propagating along the crystal surface due to the larger portion of fluorescent track contained within the excitation laser focal spot* (Bartz et al., 2014).

4.1.   *Automatic FNTD reader design*

A photo of the commercial automatic FNTD reader developed by Landauer is shown on Figure 15. The reader is produced in two variants. The first is a neutron dosimetry system (model FXR-700N) with 2D scanning performed with fast axis scanning by a single galvanometer and slow axis scanning by a translation stage. Surface position determination and setting the scan depth is performed by a piezo actuator and a high numerical aperture dry objective lens (Nikon 100×, 0.95 NA). The reader can scan and process automatically the engraved IDs and fluorescent images of up to 184 detectors on a tray according to a predetermined algorithm with configurable parameters (Akselrod et al., 2014a).

The second variant of the reader (model FXR-700R) is designed for research laboratories. It has two galvanometers for 2D scanning of the detector crystal in a static position of the tray to obtain stacks of images scanned at different depths in the crystal for 3D imaging and track trajectory reconstruction (Greilich et al., 2013; Klimpki et al., 2016). Massive scanning of multiple detectors and multiple image stacks on the same detector is easily configurable. Precise surface

position and depth of scanning setting for each detector is determined automatically by the reflection of the laser light peak position measured with a photodiode.
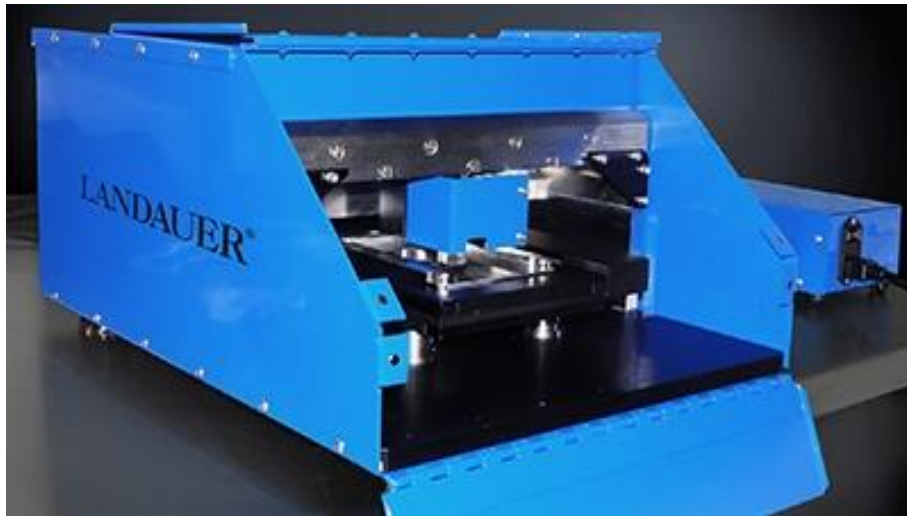

Figure 15: Commercial automatic FNTD reader produced by Landauer (Akselrod et al., 2014a).

Further improvements in FNTD instrumentation were recently achieved by introducing crystal coloration determination before starting the confocal laser scanning (Akselrod et al., 2014b). This technique allowed estimation of detector photon and neutron sensitivity for high dose analog mode without doing individual calibration by irradiating, reading and bleaching of each detector.

4.2.   Application of super-resolution microscopy techniques for FNTD imaging

Significant improvements in high resolution imaging have been made since the initial introduction of FNTDs. The resolution of CLSM is limited by the diffraction limit: the smallest detail that can be resolved using light photons. This limit is determined by the wavelengths of the excitation and emission lights and translates to approximately 240 x 240 x 940 nm^3 (x, y, z) voxels for the best available oil-emersion lenses. Over the last two decades, a number of techniques surpassing this physical limitation have become commercially available and two were used for FNTD read-out to visualize sub-micrometer sized tracks, namely structured illumination microscopy (SIM) (Gustafsson, 2000; Kouwenberg et al., 2018a) and stimulated emission depletion (STED) (Greilich et al., 2013; Hell, 2003).

STED employs two pulsed overlapping laser beams: the primary laser beam that stimulates the excitation transition of the luminescent centers and a secondary high peak power and doughnut-shaped laser beam with the wavelength corresponding to the emission transition. This second laser beam depletes (and temporarily disables) fluorescent centers excited by the primary beam within a small volume outside the center of the primary stimulation laser beam (Figure 16).
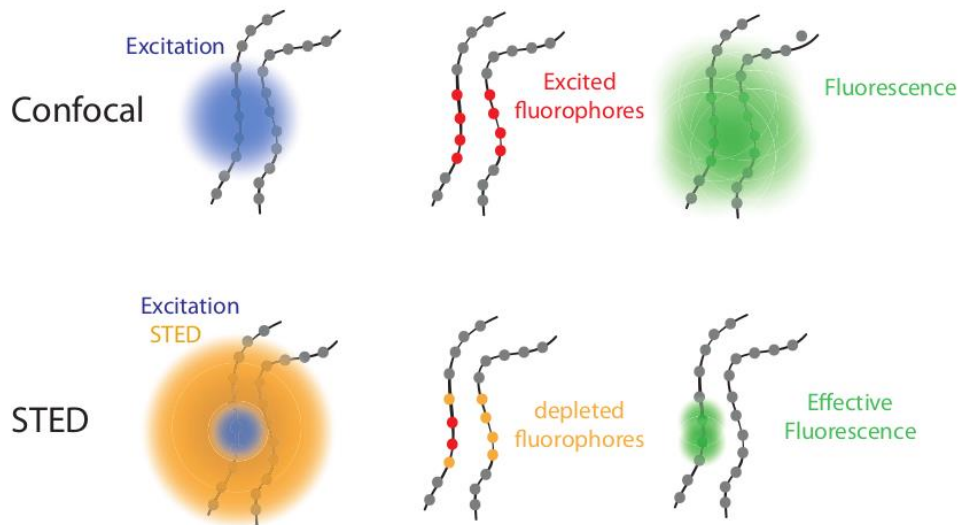
Figure 16: Illustration of the STED principle compared to CLSM for imaging of fluorophores (or fluorescent centers). While employing a similar, diffraction limited, excitation spot, the number of functioning fluorophores are reduced with STED due to quenching/depletion of excited luminescent centers on the periphery of the primary excitation beam (blue) using a donut shaped secondary depletion beam (orange) (Scientific Volume Imaging, 2017).

In STED careful adjustment of the peak power, duration and delay time between both laser beam pulses allows the reduction of the emitting volume of FNTD crystal down to 80 nm in the lateral (x,y) direction (Figure 17, left) (Niklas et al., 2017). The data collected after irradiation of FNTD crystals with ions having different LET indicates that the observed track spot widths contain information on the energy distribution when the track dimensions are larger than ~90 nm. The STED measurements identified the FWHM to be a limited proxy for the LET of individual ions, similar to the track spot intensity but less dependent on detector sensitivity. In the future STED could be an excellent candidate for 3D track imaging and validation of Monte Carlo simulations of track structure.

SIM is a wide-field microscopy technique which employs a raster of laser lines, instead of scanning a single focused laser beam, to excite the whole image plane at once. Fluorescent images obtained at various rotational positions of the excitation raster are recorded to retrieve information from the frequency space outside the observable region. This technique yields a two-fold increase in spatial resolution compared to CLSM (Figure 17, right). SIM might be faster than STED and CLSM since no raster-scanning is required but is computationally intensive in the reconstruction stage of

image processing. It was shown for alpha tracks in FNTDs that the superior resolution of SIM estimated the scattering of particles better than CLSM (Kouwenberg et al., 2018a).

The time required to scan a 100 x 100 x 10 µm FNTD volume varies greatly depending on the used methodology and required signal-to-noise ratio. SIM and CLSM are relatively fast and take between 2 and 30 minutes. STED is slow due to pulsed stimulation and multiple illumination steps and can take up to several hours for imaging at high resolutions.
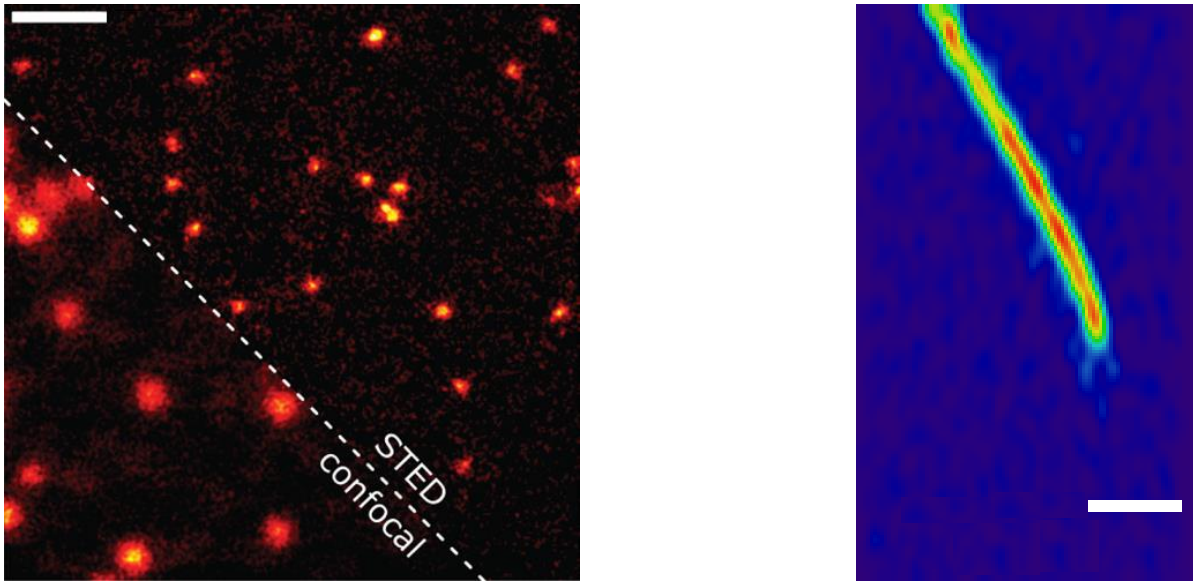

Figure 17: (left) Comparison of confocal and Stimulation Emission Depletion (STED) imaging of ion tracks in FNTD (Niklas et al., 2017). *(right) Alpha tracks imaged using Structural Illumination Microscopy (SIM)* (Kouwenberg et al., 2018a). *Scale bars are 1 µm.*

4.3. Annealing, bleaching and reusability of FNTDs

FNTDs can be read with red laser light multiple times without erasure, but at the same time the detectors can be erased and reused multiple times after thermal annealing or optical bleaching. As was shown in the Section 2.2 and Figure 8, radiation-induced fluorescent signal in FNTDs is stable up to 600 °C but can be thermally annealed to background by heating the crystals to 650 °C. Optical bleaching with pulsed UV laser light using two-photon absorption photoionization process is more effective, however, as it results in a significantly lower background fluorescent signal (see examples in Table 1). The main criteria of FNTD image quality is signal-to-noise ratio (SNR), a parameter obtained from a standard crystal sample irradiated in vacuum with [241]Am alpha particles from a 200 mm distance to produce identical tracks propagating normally to the crystal surface resulting in bright round fluorescent spots. SNR in this case is defined as the ratio of the average alpha particle fluorescent track amplitude divided by one standard deviation of the fluorescent

background surrounding the tracks. A special FNTD laser bleaching system is available from Landauer for erasing the accumulated dose before the next use of the detectors. The system allows loading up to 1000 detectors on four trays and bleaching them automatically with a bleaching time of 30 s per one detector.

Table 1: Improvements as result of different detector treatments (Sykora and Akselrod, 2010a)

Crystal state	Background fluorescence (a.u.)	Alpha track fluorescent amplitude (a.u.)	Signal-to-noise ratio
As-grown	65 ± 2	22	9.4
Annealed	235 ± 3	38	13.6
Bleached 325 nm	22 ± 1	38	40.0
Bleached 260 and 325 nm	33 ± 1	45	47.4

5. APPLICATION OF FNTD IN RADIATION DOSIMETRY

5.1. *Dosimetry of neutrons at low doses*

Personal neutron dosimetry remains the most difficult dosimetry task since no single method is able to deliver the required energy and dose response, detector sensitivity and accuracy that is necessary (ISO 21909-1:2015). One of the first applications of FNTDs was therefore measurement of neutrons. While neutrons themselves produce no detectable signal in FNTDs at low doses and neutron energies, products of nuclear reactions between neutrons and a neutron converter produce easily detectable tracks. Converters containing a high content of hydrogen, like polyethylene (PE), for fast neutron detection and ^{6}Li- and ^{10}B-containing compounds, having high neutron capture cross-section resulting in (n,α) reactions, for thermal and intermediate energy neutrons were tested. Track detectors, including FNTDs, have traditionally measured neutron dose by proportionally relating track density of nuclear reaction products to the incident neutron fluence and dose (Figure 18).
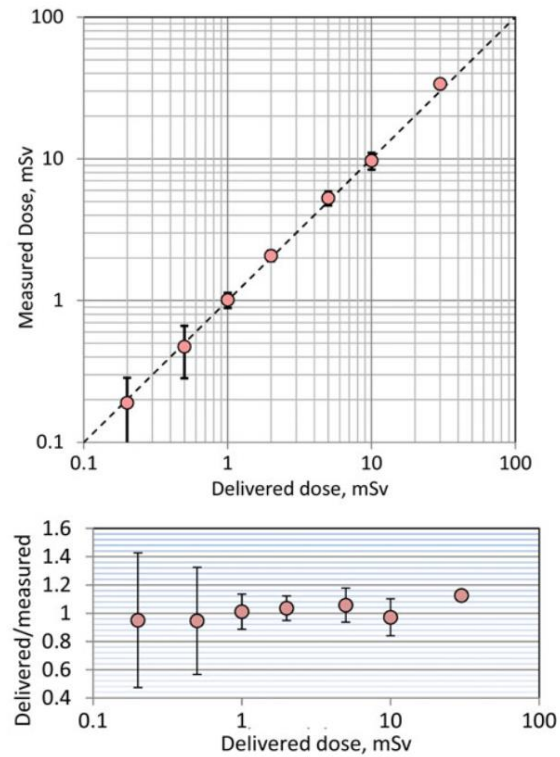
Figure 18: Measured neutron doses as a function of delivered doses (top). 1:1 line represented as a dashed line. Error bars represent 1 standard deviation. Detectors were irradiated with ^{241}AmBe neutrons. In the bottom chart, measured dose and standard deviations were normalized to the delivered dose (Akselrod et al., 2014a).

Unlike Plastic Nuclear Track Detectors (PNTD), Al_2O_3:C,Mg is also sensitive to low linear energy transfer (LET) radiation including secondary electrons resulting from interactions of photons with the crystal. Neutron radiation is usually accompanied by gamma radiation. If the dose of gamma radiation is above several cGy, then the fluorescence induced by overlapping secondary delta electron tracks can interfere with the signal induced by recoil protons making it difficult to detect and count neutron induced tracks. An advanced image processing method was developed to determine the correct dose in mixed gamma-neutrons fields (Sykora and Akselrod, 2010b).

Thermal neutrons were detected in FNTDs via the production of alpha particles and tritium ions in ^{6}LiF or ^{6}Li-glass and fast neutrons were observed via recoil protons produced in polyethylene (PE) (M. S. Akselrod et al., 2006). From their penetration depth in the FNTD, alpha particles (helium ions) were distinguished from tritium ions. A more extensive study involved irradiations using fast neutrons in air and on a PMMA phantom using PE, ^{6}LiF and ^{10}B converters and moderated neutrons with TLD-100 and TLD-600 as converters (Sykora et al., 2008b). The absorbed dose was calculated using the track density and detector sensitivity expressed in tracks per 1 mm^2 of scanned detector area per 1 mSv of neutron dose. A

linear relation between absorbed doses and track densities was observed. FNTDs proved to be superior in sensitivity to CR-39 PNTDs. Depending on the manufacturer of CR-39 plastic, FNTDs provide up to four times increase in detection efficiency and a 100 times higher saturation dose.

To tackle the strong neutron energy dependence of the detector sensitivity (Figure 19) it was proposed to use two different methods (Sykora et al., 2009). First is to calculate the ratio of track densities measured behind two converters: one made of PE and one made of a ^{6}Li-based compound (Figure 20). Estimated neutron energies were in good agreement with the reference values for median neutron energies between 40 keV and 4 MeV. The second method is to measure the track density behind a PE converter as a function of depth in the crystal, as recoil proton penetration depth depends on the initial neutron energy. This second technique produced good results for high energy neutrons in the range from 1 MeV to 19.6 MeV. (Figure 21) (Sykora et al., 2009).
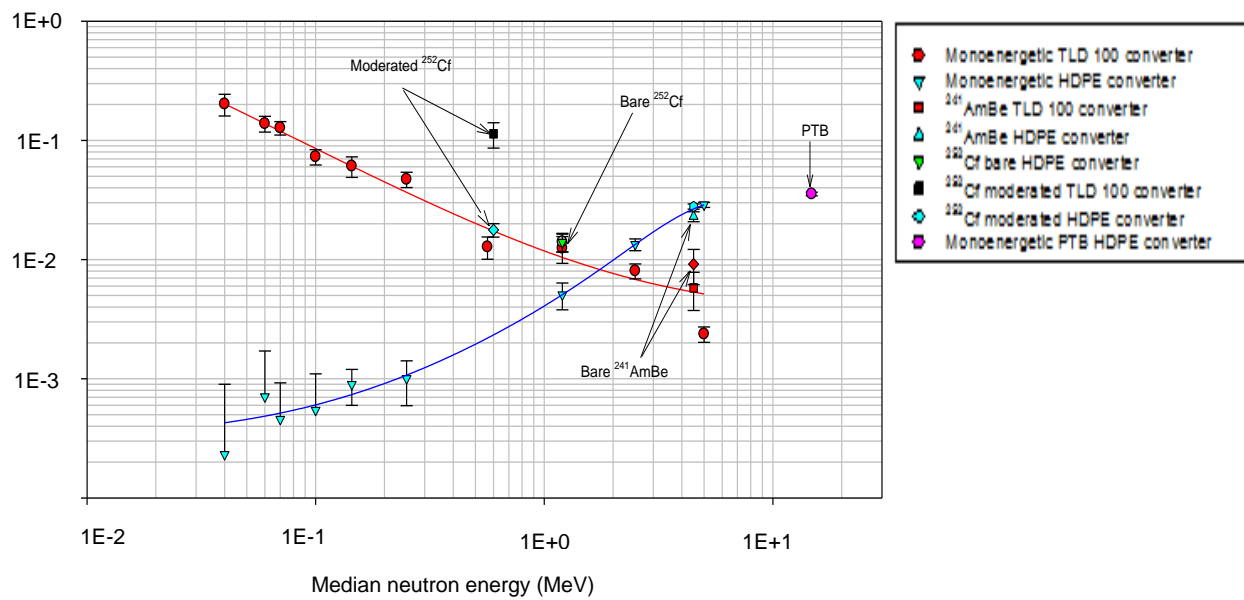

Figure 19: Neutron energy dependence of FNTDs irradiated at NPL (UK) and PTB (Germany) with mono-energetic and broad spectrum neutrons (Sykora et al., 2009).
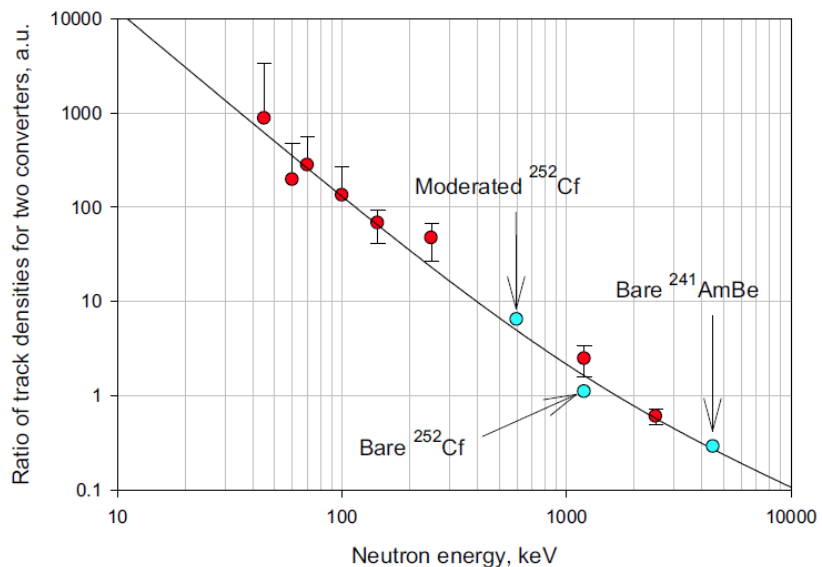
Figure 20: Track density ratio measured in FNTDs behind TLD-100 and PE converters as an estimator of neutron
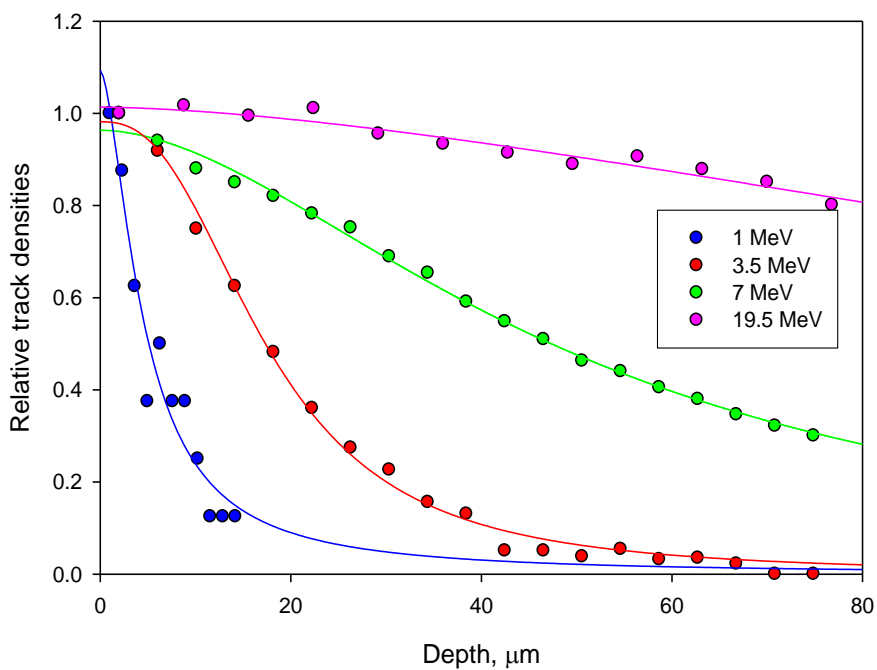
energies (Sykora et al., 2009).

Figure 21: Track densities for FNTDs covered with PE converter as a function of scanning depth for high energy

mono-energetic neutrons (Sykora et al., 2009).

5.2. *Dosimetry of neutrons at high doses*

Spatial frequency analysis of fluorescent images (Sykora and Akselrod, 2010c) provides a new approach to determine the dose of radiation through evaluation of the modulation of the fluorescence intensity within images acquired from an irradiated FNTD. The modulation of fluorescence intensity is caused by non-uniform distribution of ionization produced by charged particles (either neutron-induced recoil protons or photon-induced secondary electrons). Although gamma photons may be incident on the crystal in a uniform manner, the amount and localization of energy deposition has a microscopic and statistical variation as described by a microdosimetric approach (Rossi and Zaider, 1996).

Quantitative evaluation of fluorescence intensity modulation can be determined by spatial frequency analysis of the image illustrated by Figure 22.
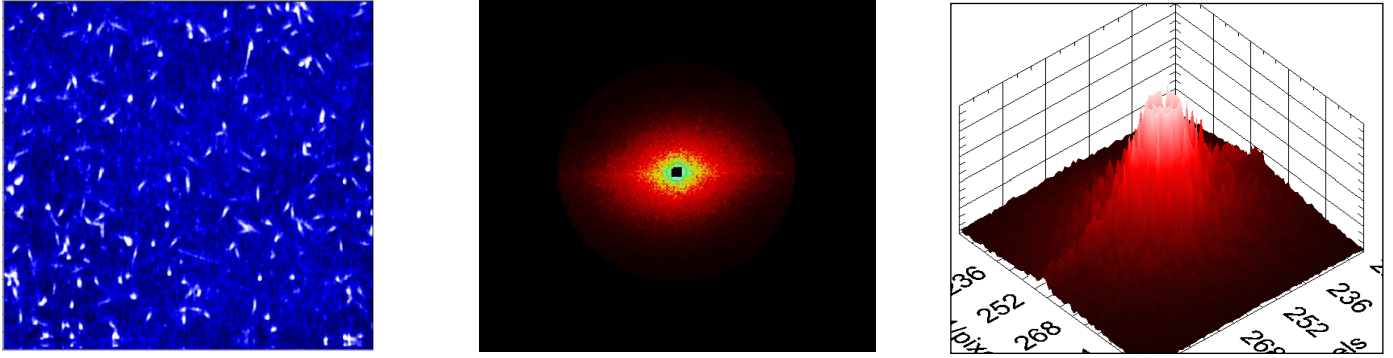

Figure 22: Processing of high photon and neutron dose images using the spatial frequency domain, Discrete Fourier Transforms and the Power Spectrum Integral as the dose-indicating parameter (Sykora and Akselrod, 2010c).

The image is converted into the spatial frequency domain by the Discrete Fourier Transform (DFT) defined by:

$$F(k,l) = \frac{1}{N^2} \sum_{m=0}^{N-1} \sum_{n=0}^{N-1} f(m,n) e^{-\frac{2\pi i}{N}(km+ln)}$$

(1)

where *f(m,n)* is the intensity of the original image in the spatial domain at points *m* and *n, k* and *l* are spatial frequencies and F(0,0) represents the DC offset of the image. The power spectral density of the image is calculated by squaring the magnitude of the Fourier transform. Integrating the power spectral density over a specially selected frequency range in the image provides the parameter – Power Spectrum Integral (PSI) – which was found to be proportional to the absorbed dose:

$$PSI = \int_{k_0}^{k} \int_{l_0}^{l} \left| f(k,l) \right|^2 dk\,dl \; \propto \; D \tag{2}$$

where k_0 and l_0 are the initial spatial frequencies of interest.

The so-called "analog" technique using PSI was successfully used to discriminate neutron- and photon-induced signal produced behind PE and PTFE converters. Signal induced in FNTDs behind a PE converter is a combination of neutron and photon doses, whereas signal behind a PTFE converter that does not contain hydrogen is proportional only to photon dose (Sykora and Akselrod, 2010b).

A linear relation between the PSI and the high neutron dose in combination with the track counting technique at low doses allows one to measure neutrons in a wide dynamic range between 0.1 mSv and 10 Sv (Figure 23) with up to a 1:3 neutron-to-gamma dose ratio. Correcting for nonlinearity of dose response, neutron and photon doses can be measured up to 30 Gy. Correction of detector sensitivity based on crystal coloration using green fluorescence intensity, a feature available in the fast automated reader, allows the user to determine the doses within +/-30% limits without individual detector calibration using radiation sources (Figure 24) (Akselrod et al., 2014a). The ability to measure mixed neutron-gamma fields over a wide energy (thermal to 20 MeV neutrons) and dose (0.1 mSv to 30 Sv) range with energy discrimination and detector reusability make the FNTD an attractive technique for personal neutron dosimetry.
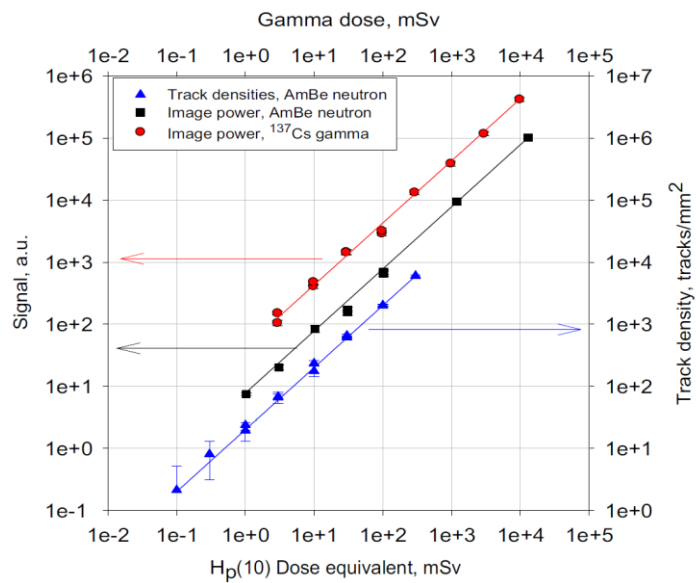

Figure 23. Dose dependences of FNTDs irradiated with neutrons and photons and measured in track counting and analog PSI mode (Sykora and Akselrod, 2010c).
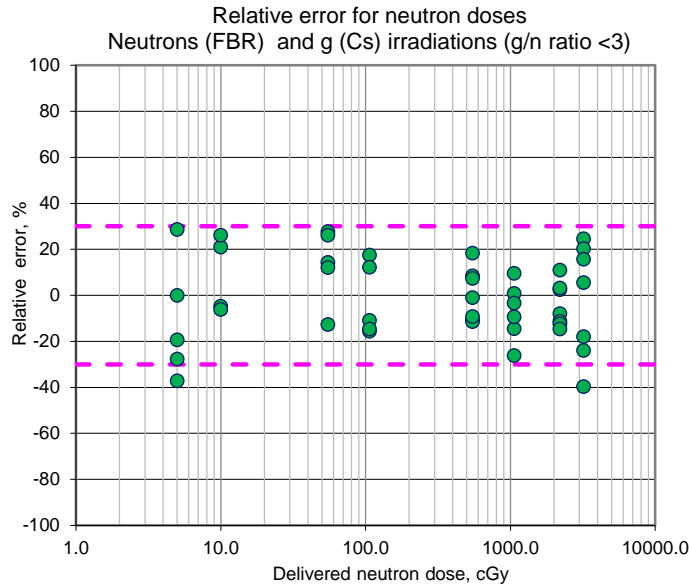
Figure 24: Uncertainties of high neutron dose determination using FNTDs with sensitivities determined by coloration measurements using blue light induced green fluorescence (Akselrod et al., 2014b).

5.3. Criticality dosimetry

Fluorescent nuclear track detectors (FNTDs) are suggested for criticality dosimetry of neutrons and photons (Harrison et al., 2017a). The depth profiles of the fluorescent signal from FNTDs after exposure to high doses of broad spectrum neutron fields from four different sources were analyzed using the power spectrum integral (PSI) measured at increasing depths within the Al_2O_3:C,Mg crystals and showed differences for the different neutron spectra (Figure 25). The depth profiles were compared to Monte Carlo simulations of energy deposition of recoil protons as a function of depth in aluminum oxide for the same four neutron sources. An algorithm for estimating the median neutron energy and neutron dose correction factors was developed and successfully tested. This algorithm includes the use of several correction and calibration functions, but the main parameter – median neutron energy – was obtained by fitting the depth profile with an exponential function and determining the depth at which the PSI value reduced $1/e$ times.
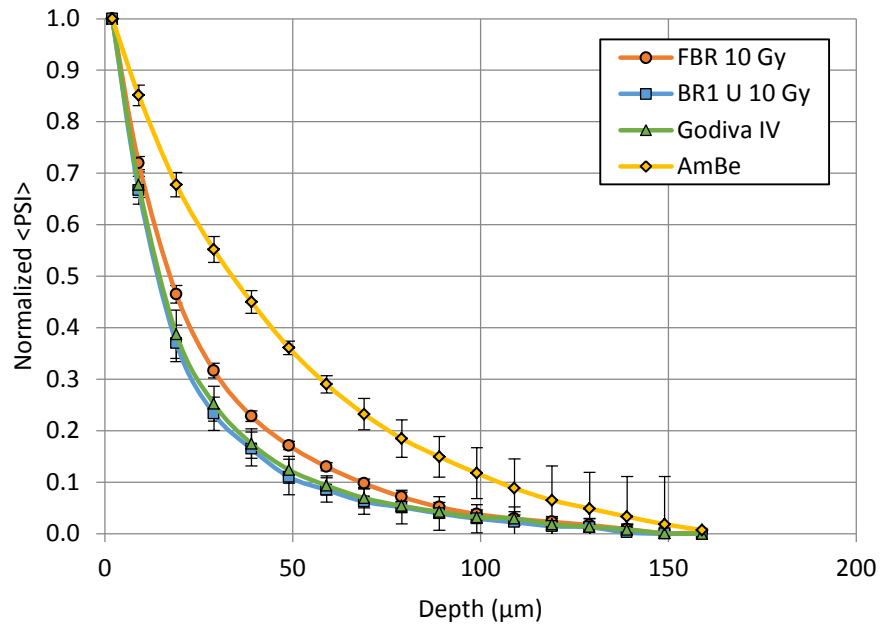
Figure 25: Experimental neutron-induced FNTD PSI signal depth profiles for four different neutron reactor spectra normalized to values obtained at 2 µm depth. The corresponding experimental uncertainties are ±1 standard deviation (Harrison et al., 2017a).

5.4.   *Gamma and X-Ray dosimetry using integral fluorescent signal*

The simplest way to measure the absorbed dose of photons using FNTDs is to use the RPL technique with 335 nm UV or 635 nm red LED illuminators and 750 nm luminescence (M.S. Akselrod and A.E. Akselrod al., 2006; Harrison et al., 2017b). The useful dose dynamic range of this type of measurement is limited relative to OSL or confocal scanning with PSI technique as it covers only 4 decades mostly due to elevated background signal even after optical bleaching (Figure 26).
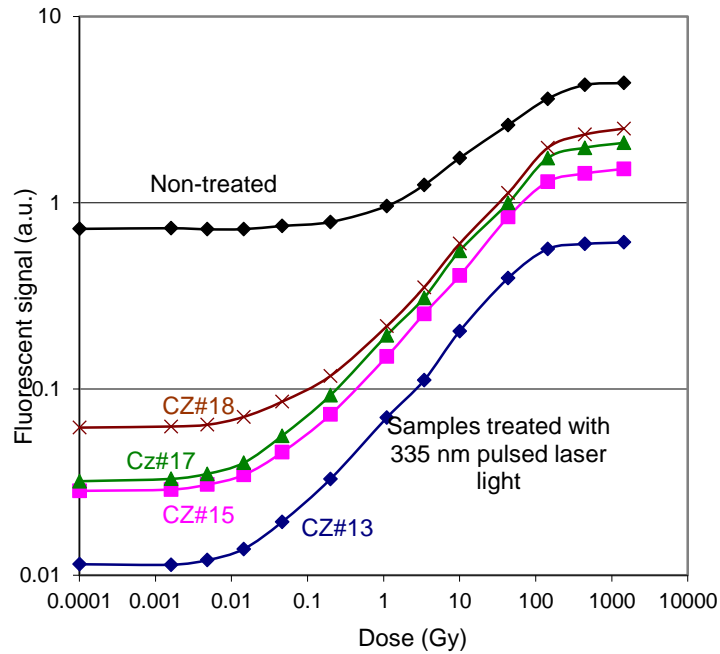
Figure 26: Dose dependence of 750 nm fluorescent light from Al₂O₃:C,Mg crystals under 337 nm excitation in as-grown (non-treated) and bleached with 335 nm pulsed laser light (M.S. Akselrod and A.E. Akselrod, 2006).

FNTDs also found application in Microbeam Radiation Therapy (MRT), where high doses of collimated, quasi-parallel arrays of synchrotron photon beams with energies between 40 and 350 keV and a peak of intensity at 90 keV are used to increase therapeutic efficiency (Bräuer-Krisch et al., 2010). In collaboration with the European Synchrotron Radiation facility in Grenoble, France, FNTDs were irradiated with 50 μm wide and 400 μm spaced microbeams with doses up to 30 Gy (Bartz et al., 2011a). A 1 μm spatial resolution of dose mapping was achieved (Figure 27) and a linear relation between fluorescence and dose was observed. The main goal of this research was to demonstrate the performance of FNTD as a quality control tool for MRT with the peak dose and peak-to-valley dose ratio as the main parameters to be monitored.
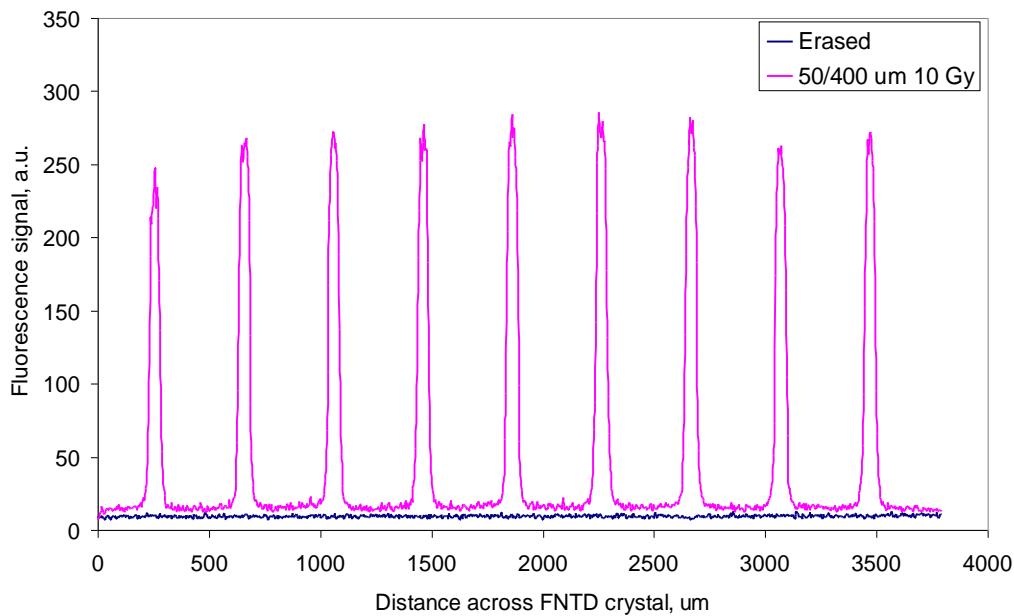
Figure 27: High resolution dose mapping of the synchrotron microbeam using FNTD (Bartz et al., 2011a).

5.5. *Imaging and dosimetry of high energy ion beams used in radiotherapy*

In radiobiology and radiotherapy research it is important not only to image and count the number of ion tracks, but it is critical to measure each incoming charged particle's LET and to estimate the contribution to dose from both the projectile and the target atom's fragments (Figure 28). FNTD technology has been successful in measuring the LET of a wide range of ions with different energies from protons to Xe ions (G. M. Akselrod et al., 2006; Bartz et al., 2014; Greilich et al., 2016; Klimpki et al., 2013; Sykora et al., 2008b). Because of the stochastic nature of energy deposition along the ion track, FNTDs need to be read using confocal scanning in stacks of 2D images (Figure 13) (G. M. Akselrod et al., 2006) where the depth spacing is limited by the optical system point spread function axial dimension. Fluorescent intensity of tracks was proposed as a measure of LET. Several corrections including track incidence angle, microscope's field of view curvature, spherical aberrations and crystal coloration non-uniformity have to be applied to minimize the LET spectral line width (Bartz et al., 2014). The minimal LET spectral line width of 2.5% at FWHM was demonstrated with 290 MeV C-ions produced by the HIMAC accelerator in Japan. Spectral lines of fragments starting from [2]He through [5]B were resolved and automatically processed by the image processing routine (Figure 31). Proton tracks were also visible but at that time could not be processed and quantized automatically.

Another parameter that was investigated as a measure of LET and atomic number Z is fluorescent track width (FWHM) (Bartz et al., 2014; Klimpki et al., 2016; Sykora et al., 2008a). Both fluorescent intensity and track width should increase

with the increase of the particle LET and Z, but measurements of a track's size are limited by the resolution of the employed microscopy technique and in the case of confocal microscopy the increase in track size is measurable only at relatively high LETs when track size exceeds the lateral size of optical system PSF. Super-high resolution microscopy may extend the range of LETs measured with the lateral track size. It is important to emphasize that FWHM of a track fundamentally should not depend on crystal properties whereas fluorescent intensity of a track strongly depends on detector crystal coloration and requires calibration of each crystal. Although the absorbed dose within the heavy ion tracks can reach hundreds of Gy there are no signs of color center saturation even at LETs above 10,000 keV/μm (Figure 29).
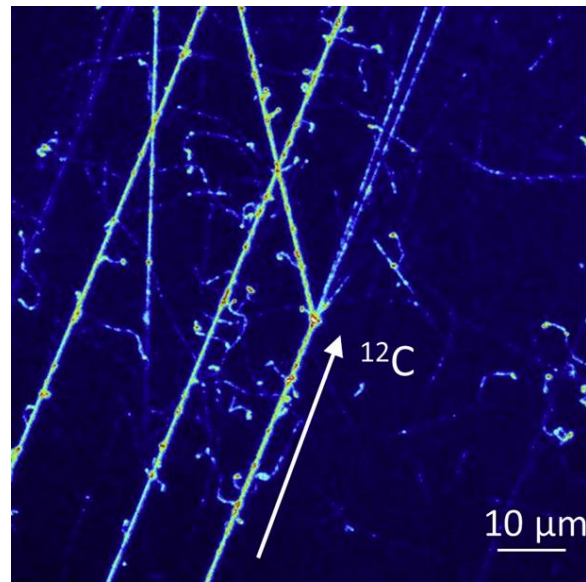
Figure 28: Example of carbon ion tracks passing through an FNTD. The arrow indicates a track of a primary carbon ion which undergoes a nuclear reaction (fragmentation). The smaller curly tracks surrounding the primary particles and fragments are high energy delta electrons. The fluorescence intensity of the track corresponds to the energy deposited in the crystal volume (Greilich et al., 2013).

Figure 29: Mean track amplitude histogram for various ions and energies in bare FNTDs (Sykora et al., 2008a).

Figure 30: LET in Al₂O₃:C,Mg versus fluorescence track amplitude. The insert shows the relation between the fluorescence track amplitude and Z/β, where Z is the effective charge of the ion and β is the relativistic ion velocity (Sykora et al., 2008a).

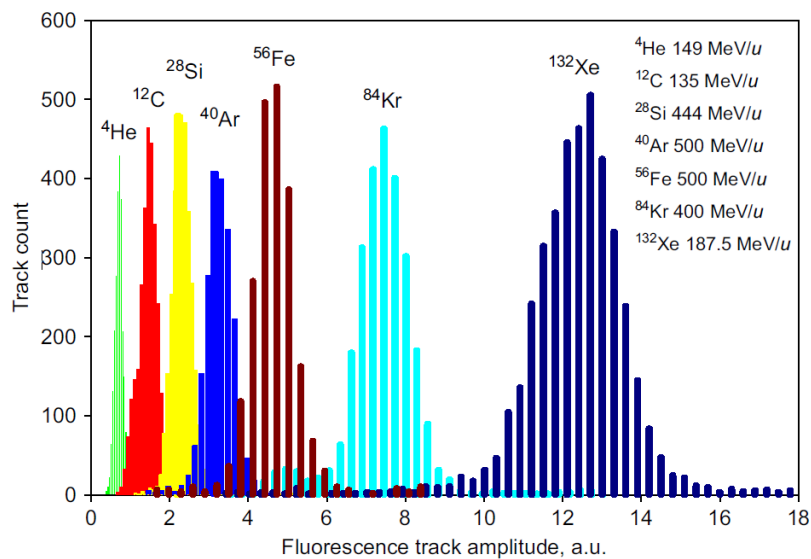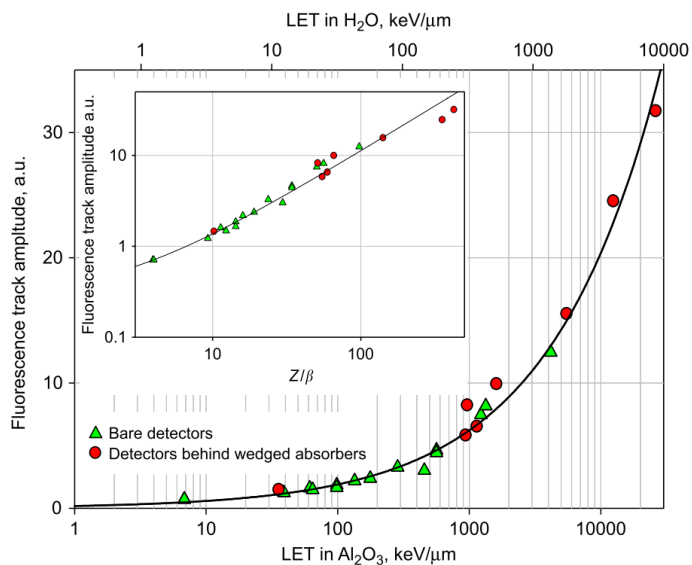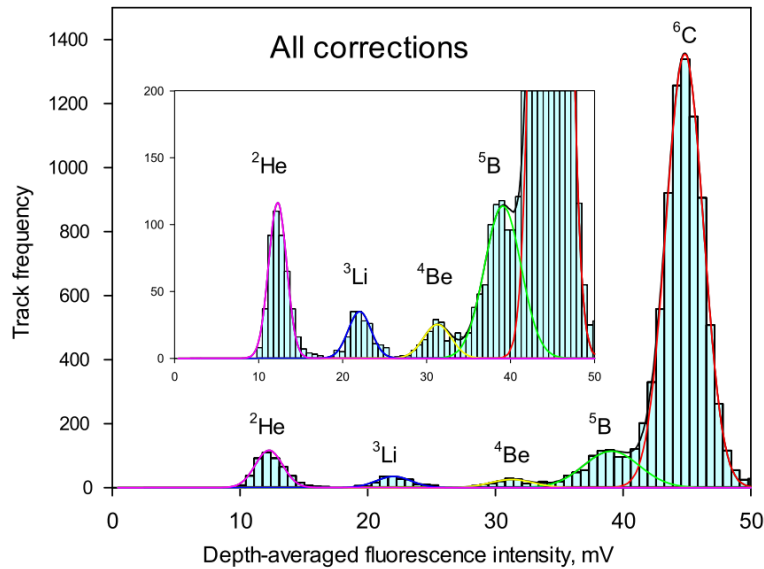*Figure 301: Spectrum of fluorescent track intensities of primary 290 MeV C-ions and their nuclear fragments produced when the carbon beam penetrates through 63 mm of PMMA absorber. The peaks corresponding to the different fragment nuclei are marked* (Bartz et al., 2014).

Various studies have been dedicated to the relation between fluorescence intensity and LET. While a direct relation between fluorescence intensity and LET was observed for protons (Bartz et al., 2011b; Sawakuchi et al., 2016), it is hypothesized that color center saturation is reached at low LETs, resulting in a complex relation between fluorescence intensity and LET for heavy ions. In addition to fluorescence increase, enlargement of the track diameter was observed for particles with $LET_\infty H_2O > 100$ keV/µm (Sykora et al., 2008a). Sykora et al. were the first to produce a direct relation between the fluorescence track amplitude, given by the average fluorescence intensity of the track, and the LET (Figure 30) for multiple ions with an $LET_\infty H_2O$ ranging from 2.2 to 8767 keV/µm (Sykora et al., 2008a). Niklas et al. showed similar results for the maximum fluorescence intensity and showed that the track diameter is related to the maximum delta ray range (Niklas et al., 2013a). Following these results, Klimpki et al. proposed a hyperbolic relation between the fluorescence intensity fluctuation, related to the stochastic nature of energy deposition of ionizing particles, and the LET (Klimpki et al., 2016). From this fluctuation of intensity, the authors concluded that the LET is best estimated from the intensity straggling below LET of 10 keV/µm. This method is advantageous compared to the track intensity approach since it is independent of FNTD sensitivity. FNTDs offer excellent measurement efficiency over a wide range of LETs and ion charges but more efforts for the standardization of LET and the ion charge calibration are required. The

introduction of the fast automated reader (Akselrod et al., 2014a) already improved this process by automating the readout, surface detection and FNTD sensitivity calibration.

In addition to fluorescence based methods, ion ranges in Al_2O_3:C,Mg have been used to estimate alpha particle energies (Bartz et al., 2013) and others (Kouwenberg et al., 2016, 2018a). The new approach reduced the measured energy uncertainty of alpha particles down to the expected straggling in Al_2O_3 and is superior to intensity based approaches since no corrections for fluorescence intensity and detector sensitivity are required. However, since the maximum depth that CLSM can reach is in the range of 200 μm, only particle beams with low energies can be measured using this technique. By irradiating the FNTD from the side and measuring the fluorescence parallel to the ion beam, Klimpki et al. reported less than 3% deviation from tabulated SRIM data for the ranges of C, Mg, S, Fe and Xe ions in the FNTD (Klimpki et al., 2013).

Several authors reported a near 100% detection efficiency of primary particles in various ion beams compared to the reference fluence and the fluence measured using CR-39 PNTDs (G. M. Akselrod et al., 2006; Osinga et al., 2013, 2014a). It was found that the fluence of secondary particles, produced by fragmentation of the primary beam, was underestimated by the FNTD approach compared to simulation. This is the result of the relatively low LET and possibly high angle of incidence of fragments (Klimpki et al., 2016). Osinga et al. showed a 5 fold underestimation of H, He and Li-fragments in a carbon beam (Osinga et al., 2014b).

Track-based dosimetry remains challenging due to the uncertainties in charge, LET and fluence. Osinga et al. reported differences in absorbed doses between a fluence-based FNTD approach, including fragments, and ionization chamber measurements of 2.4% and 4.5% for respectively 142.66 MeV protons and 270.55 MeV/u carbon ions (Osinga et al., 2014b). The mass stopping powers for the primary and secondary particles in this study were estimated in advance. Klimpki et al. employed both fluence and LET measurements to estimate the absorbed dose from a degraded carbon beam to yield a 15% deviation from the expected dose. It was assumed that the relatively large underestimation of 9% was the result of LET and angular uncertainties. The authors argued that the large number of undetected low-LET fragments might be the cause of the found deviation in dose (Klimpki et al., 2016). At higher doses and corresponding ion fluencies, the overlap of tracks becomes problematic. Sykora and Akselrod therefore proposed to use the power spectrum integral (PSI) instead of track counting for dose estimation (Sykora and Akselrod, 2010b). In this approach, the Fourier transformed special frequency spectrum of the fluorescent image is calculated and integrated excluding the lowest

frequencies to avoid background contribution. The PSI approach is able to deal with much higher doses than track counting but suffers from crystal coloration dependency of LET and requires the detectors' calibration (Bartz et al., 2014). Due to this LET dependency, significant overestimation of the absorbed dose in the Bragg peak of modulated proton beams was observed. It can therefore be concluded that FNTDs offer excellent opportunities for ion track visualization and radiobiology research via charge and LET spectroscopy, but further research is required before it can be used as an independent dosimeter in therapeutic ion beams.

6. FNTDS IN RADIOBIOLOGY

Aluminum oxide, and therefore the FNTD, is a biocompatible material which means that the detector is non-toxic and cells can grow and thrive on these detectors. This has led to some very innovative uses of FNTDs for radiobiology. In radiobiology, the damage induced in the cell, and mainly in the DNA, is of major importance in improving the effectiveness of the radiotherapy treatment of cancerous tissue and reducing the chance of inducing secondary cancer in healthy tissue. Niklas et al. were the first to combine FNTDs with cell cultures on top of the detector to create a hybrid detector (Cell-Fit-HD) (Niklas et al., 2013b). Various fluorescent markers for cell organelles, nuclei and damages induced in the DNA are commercially available. Tracks in the FNTD, cell geometry and DNA damage can therefore be measured using CLSM and a single hybrid detector. FNTDs covered with human lung adenocarcinoma epithelial (A549) cells, a type of lung cancer, were irradiated using a 270.5 MeV/u carbon beam. The cell nuclei were visualized using HOECHST staining, γ-H2AX staining and Double Strand Breaks (DSB), a form of DNA damage which is hard to repair and likely to induce cell death. This required the cells to be killed and fixated before imaging. By imaging both the cell layer and the FNTD after irradiation, the induced DNA damage could be determined on a per-track basis (Figure 31).
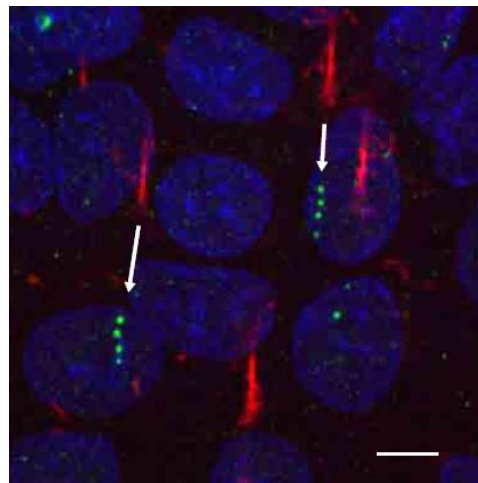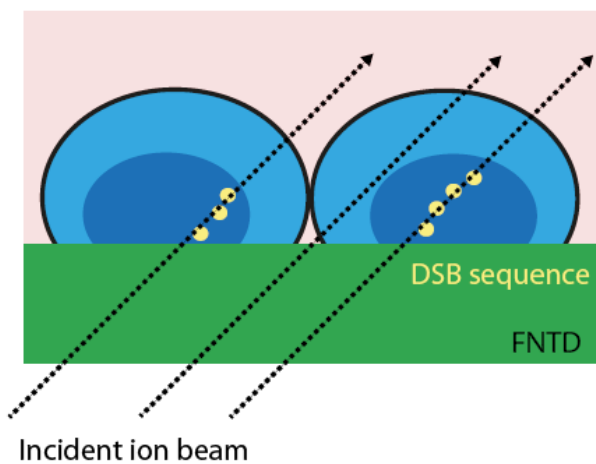
Figure 31: (left) Schematic depiction of the acquired FNTD stack proximate to the detector surface. The arrows connect the DSB sequences with the corresponding ion tracks. (right) A superposition of cellular response as a maximum intensity z-projection; blue: nuclei, red: FNTD tracks, green: g-H2AX foci as an indicator of DNA double strand breaks. Scale bar is 5 μm (Niklas et al., 2013b).

Other studies involved more cell types and staining to produce similar results (Niklas et al., 2013c). Kodaira et al. showed that the Cell-Fit-HD approach also works in live cells when using 53BP1-GFP staining (Figure 323), which was an important step required to allow the study of DNA damage and repair over time (Kodaira et al., 2015). The Cell-Fit-HD tool was later extended to include clonogenic survival studies (Dokic et al., 2015). These studies look at the fraction of cells surviving a radiation treatment and generally require a large number of cells for statistical significance. The dose to cells and related DNA damage was estimated from the ion tracks in the whole FNTD and the formation of colonies was followed over time. This approach allows the user to study the fate of individual cells and determine factors involved in the survival or death of cells.
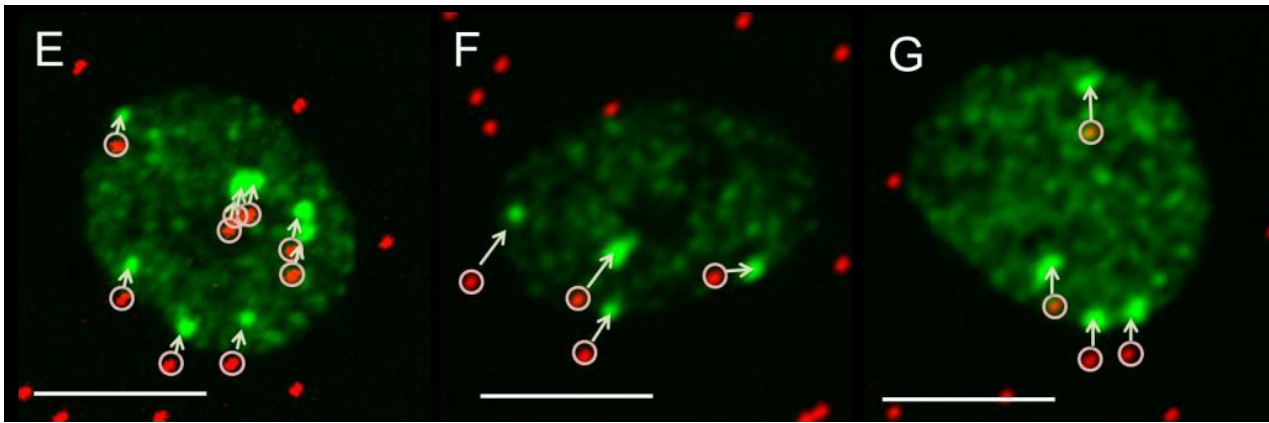
Figure 323: Co-localization of double strand breaks and ion tracks using FNTDs in HT1080 fibrosarcoma cells. The DNA DSBs are given in green while the red dots indicate neon ion tracks. Scale bars are 10 µm. The difference in position of the DNA damage and neon ion track spots was caused by cell movement between irradiation and imaging, a natural process unrelated to the FNTD surface or imaging technique (Kodaira et al., 2015).

McFadden et al. built a custom first-of-its-kind CLSM that could be placed in a beamline (McFadden et al., 2016). Utilizing fast scanning of the FNTD and cell layer enabled the authors to follow the formation of DNA damage induced by proton radiation in near real-time using their unique experimental setup (Figure 33). For radiobiology studies the FNTD crystals became available in various sizes and thicknesses down to 100 µm to better accommodate biological experiments in incubator sample holders able to keep the mammalian cells at 36 ℃ temperature (Figure 33, bottom left).

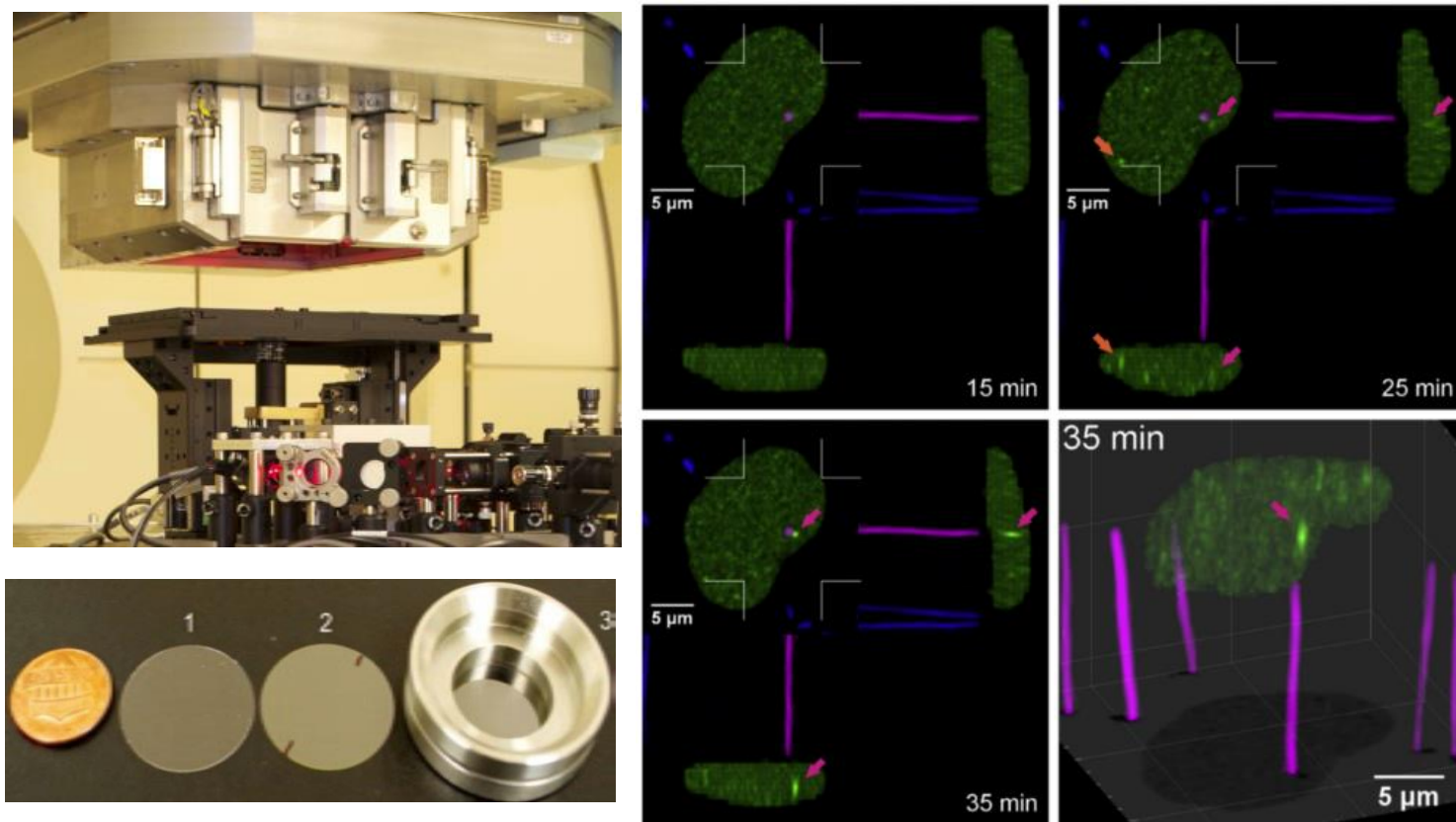*Figure 334: (left) Custom-made confocal laser scanning microscope placed in the beamline of the Proton Therapy Center-Houston, USA. (bottom) water tight incubator chamber equipped with 25 mm in diameter and 110 µm thick FNTD crystal. (right) Proton tracks (purple) passing through a HT1080 cell nucleus and evaluation of DSB foci (green) over time. Blue - extraneous tracks that do not produce foci; Crosshairs - the field of view for the perpendicular projections; Magenta arrows - proton track-induced foci; Orange arrows - non-proton track-induced foci (McFadden et al., 2016).*

Niklas et al. recently adapted the Cell-Fit-HD approach to image the cell layer using wide-field microscopy instead of CLSM. This greatly reduced the imaging time and phototoxicity (Niklas et al, 2016). This allows for cell kinetics studies on a larger time scale than was possible using only CLSM and offers a great opportunity for DNA repair and RBE studies (Dokic et al., 2016), which are considered the fields that require more research for effective heavy ion radiotherapy.

For alpha radiations, where the very short range of alpha particles prevent dosimetry methods akin to the techniques described above, Kouwenberg et al. developed a method using U87 Glioblastoma cell imaging with a large density of alpha tracks measured using FNTDs to determine the dose distribution within the nucleus of U87 cell monolayers (Kouwenberg, 2018b).

It is expected that the described techniques involving FNTD technology will have a significant impact on the field of ion radiobiology. The ability to visualize and follow the development and repair of radiation induced damage should help to unravel the complex mechanism involved in radiation induced cell death. The death and repair mechanisms play an important role in the precise determination of the radiation quality and in the design of targeted therapy where moderation of the repair mechanism in cancerous cells can greatly increase the treatment efficiency and therapeutic margin - the amount of effective dose that can safely be deposited in target sites before unwanted side-effects occur.

7. CONCLUSIONS AND OUTLOOK

While initially designed for optical data storage, the unique Al_2O_3:C,Mg-based fluorescent nuclear track detector has grown to become a diverse tool in radiation dosimetry. FNTDs utilize the radiochromic transformations of color centers to visualize the traversal of ionizing particles at a sub-micrometer resolution. Optical and thermal stability of these color centers allows for non-destructive read-out without the need for etching or post-processing, and the detectors can be stored for years without a loss of signal. Together with the reusability after optical bleaching, FNTDs offer significant advantages over other radiation detection techniques. Their small size and physical robustness provide important advantages for numerous applications in radiation dosimetry and spectroscopy.

Utilization of confocal laser scanning fluorescent microscopy for sub-micrometer imaging of the detectors is novel and allows the user to visualize energy depositions in the crystal in 3D with great accuracy. With the introduction of an automated FNTD reader, investigators' time required to image a single or multiple detectors has greatly been reduced, paving the way for large scale commercialization of the technology in neutron dosimetry and fundamental research. Additionally, two super-resolution techniques have been successfully used to image ion tracks within the FNTD at below 100 nanometer resolution, providing a valuable tool for future validation of complex Monte Carlo simulations of ion track structures and novel microdosimetric models.

A large number of publications studying the characteristics of FNTDs after irradiation with photons, neutrons and high energy ions have been produced over the past decade. It has been shown that FNTDs are able to discriminate fast and moderated neutrons and can separate neutron and gamma doses in mixed neutron-gamma fields over a wide dose range from 100 µSv to 30 Sv. Using fluorescence intensity, spot size and/or straggling within the fluorescent tracks, various authors were able to discriminate particle charge and LET in both proton and heavy ions with a near 100% detection

efficiency. The detectors have also been successfully used for the quality assurance of synchrotron microbeams and ion beams.

There are still numerous challenges and improvements expected from FNTD technology. Advances in crystal growth should improve the uniformity of crystals coloration and reduction of background signal. Faster readout instrumentation and more sophisticated image processing software should improve detectability and spectroscopy of low LET protons and even delta electrons.

The biggest advances are expected in radiobiological use of FNTDs where cell-cultures stained with fluorescent markers grown on top of biologically inert Al_2O_3:C,Mg crystals can be irradiated and imaged in real time or post factum. Ion tracks, imaged by FNTD, and DNA double-strand breaks were already successfully co-localized both after cell fixation and with living cells in real-time. This new type of hybrid detector is expected to have a large impact on the field of radiobiology where the ability to relate ion traversals with corresponding charge and LET to induced radiation damage over time can shed light on the complex mechanism of DNA damage repair and radiation quality. With these rapid developments over the last few years, further developments for the coming years can be expected.

8. AKNOWLEDGEMENT

9. REFERENCES

Akselrod, M.S., Kortov, V.S., Kravetsky, D.J., Gotlib, V.., 1990. Highly Sensitive Thermoluminescent Anion-Defective Alpha-Al203: C Single Crystal Detectors. *Radiat. Prot. Dosimetry*, 32(1) 15-20.

Akselrod, M.S., Lucas, A.C., Polf, J.C., McKeever, S.W.S., 1998. Optically stimulated luminescence of Al2O3. *Radiat. Meas.* 29(3), 391–399. https://doi.org/10.1016/S1350-4487(98)00061-4

Akselrod, M.S., Akselrod, A.E., Orlov, S.S., Sanyal, S., Underwood, T.H., 2003. Fluorescent aluminum oxide crystals for volumetric optical data storage and imaging applications. *J. Fluoresc.* 13, 503–511.

Akselrod, M.S., Akselrod, A.E., 2006. New Al2O3:C,Mg crystals for radiophotoluminescent dosimetry and optical

imaging. *Radiat. Prot. Dosimetry* 119(1–4), 218–221. https://doi.org/10.1093/rpd/nci663

Akselrod, G.M., Akselrod, M.S., Benton, E.R., Yasuda, N., 2006. A novel Al2O3 fluorescent nuclear track detector for heavy charged particles and neutrons. *Nucl. Instr. Methods B* 247(2), 295–306. https://doi.org/10.1016/j.nimb.2006.01.056

Akselrod, M.S., Yoder, R.C., Akselrod, G.M., 2006. Confocal fluorescent imaging of tracks from heavy charged particles utilising new Al2O3:C,Mg crystals. *Radiat. Prot. Dosimetry* 119(1–4), 357–362. https://doi.org/10.1093/rpd/nci664

Akselrod, M.S., Sykora, G.J., 2011. Fluorescent nuclear track detector technology - A new way to do passive solid state dosimetry. *Radiat. Meas.* 46(12), 1671–1679. https://doi.org/10.1016/j.radmeas.2011.06.018

Akselrod, M.S., Bruni, F.J., 2012. Modern trends in crystal growth and new applications of sapphire. *J. Cryst. Growth* 360(1), 134–145. https://doi.org/10.1016/j.jcrysgro.2011.12.038

Akselrod, M.S., Fomenko, V.V., Bartz, J.A., Haslett, T.L., 2014a. Automatic neutron dosimetry system based on Fluorescent Nuclear Track Detector Technology. *Radiat. Prot. Dosimetry* 161(1), 86–91.

Akselrod, M.S., Fomenko, V.V., Bartz, J.A., Ding, F., 2014b. FNTD radiation dosimetry system enhanced with dual-color wide-field imaging. *Radiat. Meas.* 71, 166–173. https://doi.org/10.1016/j.radmeas.2014.05.026

Aydarous, A., Ghazaly, M. El, 2013. Characterization of HD-V2 Gafchromic Film for Measurement of Spatial Dose Distribution from Alpha Particle of 5.5 MeV. *Int. J. Math. Comput. Phys. Electr. Comput. Eng.* 7(7), 1279–1281.

Back, T., Jacobsson, L., 2010. The alpha-Camera: A Quantitative Digital Autoradiography Technique Using a Charge-Coupled Device for Ex Vivo High-Resolution Bioimaging of alpha-Particles. *J. Nucl. Med.* 51(10), 1616–1623. https://doi.org/10.2967/jnumed.110.077578

Bartz, J.A., Sykora, G.J., Bräuer-Krisch, E., Akselrod, M.S., 2011a. Imaging and dosimetry of synchrotron microbeam with aluminum oxide fluorescent detectors. *Radiat. Meas.* 46(12), 1936–1939. https://doi.org/10.1016/j.radmeas.2011.04.003

Bartz, J.A., Sykora, G.J., Underwood, T.H., Nichiporov, D.N., Sawakuchi, G.O., Akselrod, M.S., 2011b. Evaluation of aluminum oxide fluorescent and OSL detectors in proton radiotherapy beams. *Radiat. Meas.* 46(12), 1974–1978. https://doi.org/10.1016/j.radmeas.2011.05.047

Bartz, J.A., Zeissler, C.J., Fomenko, V.V., Akselrod, M.S., 2013. An imaging spectrometer based on high resolution

microscopy of fluorescent aluminum oxide crystal detectors. *Radiat. Meas.* 56, 273–276. https://doi.org/10.1016/j.radmeas.2013.01.041

Bartz, J.A., Kodaira, S., Kurano, M., Yasuda, N., Akselrod, M.S., 2014. High resolution charge spectroscopy of heavy ions with FNTD technology. *Nucl. Instr. Methods B* 335, 24–30. https://doi.org/10.1016/j.nimb.2014.05.019

Böhm, J., Ambrosi, P., Wernli, C., 1991. Measurement of the Depth-Dose Curve of 240Pu Alpha Particles. *Radiat. Prot. Dosimetry* 39(1), 191–194. https://doi.org/10.1017/CBO9781107415324.004

Boutillon, M., 1998. Volume recombination parameter in ionization chambers. *Phys. Med. Biol.* 43(8), 2061-72. https://doi.org/10.1088/0031-9155/43/8/005

Bradley, P.D., Rosenfield, A.B., Zaider, M., 2001. Solid state microdosimetry. *Nucl. Instr. Methods B* 184(1-2), 135-57. https://doi.org/10.1016/S0168-583X(01)00715-7

Bräuer-Krisch, E., Rosenfeld, A., Lerch, M., Petasecca, M., Akselrod, M.S., Sykora, G.J., Bartz, J.A., Ptaszkiewicz, M., Olko, P., Berg, A., Wieland, M., Doran, S., Brochard, T., Kamlowski, A., Cellere, G., Paccagnella, A., Siegbahn, E.A., Prezado, Y., Martinez-Rovira, I., Bravin, A., Dusseau, L., Berkvens, P., 2010. Potential high resolution dosimeters for MRT. *AIP Conf. Proc.* 1266, 89–97. https://doi.org/10.1063/1.3478205

Cartwright, B.G., Shirk, E.K., and Price, P.B., 1978. A nuclear-track-recording polymer of unique sensitivity and resolution. *Nucl. Instr. and Methods*, 153(2-3) 457-460.

Cassou, R.M. and Benton, E.V.,1978. Properties and applications of CR-39 polymeric nuclear track detector. *Nuclear Track Detection,* 2(3) 173-179.

Chaudhuri, S.K., Zavalla, K.J., Mandal, K.C., 2013. High resolution alpha particle detection using 4H-SiC epitaxial layers: Fabrication, characterization, and noise analysis. *Nucl. Instr. Methods Phys. Res. A* 728, 97–101. https://doi.org/10.1016/j.nima.2013.06.076

d'Errico, F., 2001 Radiation dosimetry and spectrometry with superheated emulsions, *Nucl. Instr. Methods B*, 184 (1–2) 229-254.

Diaspro, A., 2001. Confocal and Two-Photon Microscopy: Foundations, Applications and Advances. Wiley-Liss.

Dokic, I., Niklas, M., Zimmermann, F., Mairani, A., Seidel, P., Krunic, D., Jäkel, O., Debus, J., Greilich, S., Abdollahi, A., 2015. Correlation of Particle Traversals with Clonogenic Survival Using Cell-Fluorescent Ion Track Hybrid Detector. *Front. Oncol.* 5, 275. https://doi.org/10.3389/fonc.2015.00275

Dokic, I., Mairani, A., Niklas, M., Zimmermann, F., Jäkel, O., Debus, J., Haberer, T., Abdollahi, A., 2016. Next generation multi-scale biophysical characterization of high precision cancer particle radiotherapy using clinical proton , helium- , carbon- and oxygen ion beams. *Oncotarget* 7(35), 56676–56689. https://doi.org/10.18632/oncotarget.10996

Evans, B.D., Stapelbroek, M., 1978. Optical Properties of the F+-center in Crystalline Al2O3. *Phys. Rev. B* 18(12), 7089–7098.

Greilich, S., Osinga, J.M., Niklas, M., Lauer, F.M., Klimpki, G.M., Bestvater, F., Bartz, J.A., Akselrod, M.S., Jäkel, O., 2013. Fluorescent nuclear track detectors as a tool for ion-beam therapy research. *Radiat. Meas.* 56, 267–272. https://doi.org/10.1016/j.radmeas.2013.01.033

Greilich, S., Jansen, J., Klimpki, G.M.., Kouwenberg, J.J.M., Neuholz, A., Pfeiler, T., Rahmanian, S., Stadler, A., Ulrich, L., 2016. Dosimetry for ion-beam therapy using fluorescent nuclear track detectors and an automated reader. 1–36, arXiv:1610.05054.

Gustafsson, M.G.L., 2000. Surpassing the lateral resolution limit by a factor of two using structured illumination microscopy. *J. Microsc.* 198(2), 82–87. https://doi.org/10.1046/j.1365-2818.2000.00710.x

Harrison, J., Moreno, B., Van Hoey, O., Mihailescu, L.C., Vanhavere, F., Million, M., Fomenko, V., Akselrod, M.S., 2017a. Characterization of fluorescent nuclear track detectors as criticality dosimeters. *Radiat. Meas.* In press, Available online Mar 27 2017. https://doi.org/10.1016/j.radmeas.2017.03.036

Harrison, J., Moreno, B., van Hoey, O., Mihailescu, L.C., Vanhavere, F., Million, M., Fomenko, V. V., Akselrod, M.S., 2017b. Characterization of fluorescent nuclear track detectors as criticality dosimeters II. *Radiat. Prot. Dosimetry* In press, Available online Oct 21 2017.

Hell, S.W., 2003. Toward fluorescence nanoscopy. *Nat. Biotechnol.* 21(11), 1347–1355. https://doi.org/10.1038/nbt895

ISO-21909-1:2015 standard, Passive neutron dosimetry systems - Part 1: Performance and test requirements for personal dosimetry

Kanai, T., Sudo, M., Matsufuji, N., Futami, Y., 1998. Initial recombination in a parallel-plate ionization chamber exposed to heavy ions. *Phys. Med. Biol.* 43(12), 3549-58. https://doi.org/10.1088/0031-9155/43/12/012

Karger, C.P., Jäkel, O., Palmans, H., Kanai, T., 2010. Dosimetry for ion beam radiotherapy. *Phys. Med. Biol.* 55(21), 193-243. https://doi.org/10.1088/0031-9155/55/21/R01

Klimpki, G.M., Osinga, J.M., Herrmann, R., Akselrod, M.S., Jäkel, O., Greilich, S., 2013. Ion range measurements using fluorescent nuclear track detectors. *Radiat. Meas.* 56, 342–346. https://doi.org/10.1016/j.radmeas.2013.03.014

Klimpki, G.M., Mescher, H., Akselrod, M.S., 2016. Fluence-based dosimetry of proton and heavier ion beams using single track detectors. *Phys. Med. Biol.* 61(3), 1021–1040.

Kodaira, S., Konishi, T., Kobayashi, A., Maeda, T., Farizal, T.A., Ahmad, T., Yang, G., Akselrod, M.S., Furusawa, Y., Uchihori, Y., 2015. Co-visualization of DNA damage and ion traversals in live mammalian cells using fluorescent nuclear track detector. *J. Radiat. Res.* 56(2), 360–365. https://doi.org/10.1093/jrr/rru091

Kouwenberg, J.J.M., Ulrich, L., Jäkel, O., Greilich, S., 2016. A 3D feature point tracking method for ion radiation. *Phys. Med. Biol.* 61(11), 4088–4104. https://doi.org/10.1088/0031-9155/61/11/4088

Kouwenberg, J.J.M., Kremers, G.J., Slotman, J.A., Wolterbeek, H.T., Houtmuller, A.B., Denkova, A.G., Bos, A.J.J., 2018a. Alpha particle spectroscopy using FNTD and SIM super-resolution microscopy. *J. Microsc.* Feb 2. https://10.1111/jmi.12686

Kouwenberg, J.J.M., Wolterbeek, H.T., Denkova, A.G., Bos, A.J.J., 2018b. Fluorescent Nuclear Track Detectors for Alpha Radiation Microdosimetry. *Radiat. Oncol. (in print)*

Lee, K.H., Crawform, J.H., 1979. Luminescence of the F-center in Sapphire. *Phys. Rev. B* 19(6), 3217–3221.

McFadden, C.H., Hallacy, T.M., Flint, D.B., Granville, D.A., Asaithamby, A., Sahoo, N., Akselrod, M.S., Sawakuchi, G.O., 2016. Time-Lapse Monitoring of DNA Damage Colocalized With Particle Tracks in Single Living Cells. *Int. J. Radiat. Oncol. Biol. Phys.* 96(1), 221–227. https://doi.org/10.1016/j.ijrobp.2016.04.007

Niklas, M., Melzig, C., Abdollahi, A., Bartz, J.A., Akselrod, M.S., Debus, J., Jäkel, O., Greilich, S., 2013a. Spatial correlation between traversal and cellular response in ion radiotherapy - Towards single track spectroscopy. *Radiat. Meas.* 56, 285–289. https://doi.org/10.1016/j.radmeas.2013.01.060

Niklas, M., Abdollahi, A., Akselrod, M.S., Debus, J., Jäkel, O., Greilich, S., 2013b. Subcellular spatial correlation of particle traversal and biological response in clinical ion beams. *Int. J. Radiat. Oncol. Biol. Phys.* 87(5), 1141–1147. https://doi.org/10.1016/j.ijrobp.2013.08.043

Niklas, M., Greilich, S., Melzig, C., Akselrod, M.S., Debus, J., Jäkel, O., Abdollahi, A., 2013c. Engineering cell-fluorescent ion track hybrid detectors. *Radiat. Oncol.* 8(141), 1-10. https://doi.org/10.1186/1748-717X-8-141

Niklas, M., Zimmermann, F., Schlegel, J., Schwager, C., Debus, J., Jäkel, O., et al, 2016. Registration procedure for spatial correlation of physical energy deposition of particle irradiation and cellular response utilizing cell-fluorescent ion track hybrid detectors. *Phys. Med. Biol.* 61(17), 441–60. doi:10.1088/0031-9155/61/17/N441.

Niklas, M., Henrich, M., Jäkel, O., Engelhardt, J., Abdollahi, A., Greilich, S., 2017. STED microscopy visualizes energy deposition of single ions in a solid-state detector beyond diffraction limit. *Phys. Med. Biol.* 62(9), N180–N190. https://doi.org/10.1088/1361-6560/aa5edc

Osinga, J.M., Akselrod, M.S., Herrmann, R., Hable, V., Dollinger, G., Jäkel, O., Greilich, S., 2013. High-accuracy fluence determination in ion beams using fluorescent nuclear track detectors. *Radiat. Meas.* 56, 294–298. https://doi.org/10.1016/j.radmeas.2013.01.035

Osinga, J.M., Ambrožová, I., Pachnerová-Brabcová, K., Akselrod, M.S., Jäkel, O., Davídková, M., Greilich, S., 2014a. Single track coincidence measurements of fluorescent and plastic nuclear track detectors in therapeutic carbon beams. *J. Instrum.* 9, P04013. https://doi.org/http://dx.doi.org/10.1088/1748-0221/9/04/P04013

Osinga, J.M., Brons, S., Bartz, J.A., Akselrod, M.S., Jäkel, O., Greilich, S., 2014b. Absorbed dose in ion beams : Comparison of ionization- and fluence-based measurements. *Radiat. Prot. Dosimetry* 161(1–4), 387–392. https://doi.org/10.1093/rpd/ncu004

Oster, L., Horowitz, Y.S., Podpalov, L., 2010. OSL and TL in TLD-100 following alpha and beta irradiation: Application to mixed-field radiation dosimetry. *Radiat. Meas.* 45(10), 1130–1133. https://doi.org/10.1016/j.radmeas.2010.06.017

Piesch, E., Burgkhardt B., 1985. Albedo neutron dosimetry. *Radiat. Prot. Dosim.* 10 (1-4) 175–188.

Ramirez, R., Tardio, M., Gonzalez, R., Chen, Y., Kokta, M.R., 2005. Photochromism of vacancy-related defects in thermochemically reduced alpha-Al2O3: Mg single crystals. *Appl. Phys. Lett.* 86(8), 1–3. https://doi.org/10.1063/1.1870130

Rossi, H.H., Zaider, M., 1996. Microdosimetry and Its Applications. Springer-Verlag, Berlin.

Sanyal, S., Akselrod, M.S., 2005. Anisotropy of optical absorption and fluorescence in Al2 O3: C,Mg crystals. *J. Appl. Phys.* 98(3). https://doi.org/10.1063/1.1999032

Sawakuchi, G.O., Ferreira, F.A., McFadden, C.H., Hallacy, T.M., Granville, D.A., Sahoo, N., Akselrod, M.S., 2016. Nanoscale measurements of proton tracks using fluorescent nuclear track detectors. *Med. Phys.* 43(5), 2485–2490.

https://doi.org/10.1118/1.4947128

Scientific Volume Imaging, 2017. https://svi.nl/STEDMicroscopy [WWW Document].

Sykora, G.J., Akselrod, M.S., Salasky, M., Marino, S.A., 2007. Novel Al2O3:C,Mg Fluorescent Nuclear Track Detectors for Passive Neutron Dosimetry. *Radiat. Prot. Dosimetry* 126(1–4), 278–283.

Sykora, G.J., Akselrod, M.S., Benton, E.R., Yasuda, N., 2008a. Spectroscopic properties of novel fluorescent nuclear track detectors for high and low LET charged particles. *Radiat. Meas.* 43, 422–426. https://doi.org/10.1016/j.radmeas.2007.11.009

Sykora, G.J., Salasky, M., Akselrod, M.S., 2008b. Properties of novel fluorescent nuclear track detectors for use in passive neutron dosimetry. *Radiat. Meas.* 43(2–6), 1017–1023. https://doi.org/10.1016/j.radmeas.2007.12.038

Sykora, G.J., Akselrod, M.S., Vanhavere, F., 2009. Performance of fluorescence nuclear track detectors in mono-energetic and broad spectrum neutron fields. *Radiat. Meas.* 44(9–10), 988–991. https://doi.org/10.1016/j.radmeas.2009.10.027

Sykora, G.J., Akselrod, M.S., 2010a. Photoluminescence study of photochromically and radiochromically transformed Al2O3:C,Mg crystals used for fluorescent nuclear track detectors. *Radiat. Meas.* 45(3–6), 631–634. https://doi.org/10.1016/j.radmeas.2009.11.022

Sykora, G.J., Akselrod, M.S., 2010b. Novel fluorescent nuclear track detector technology for mixed neutron-gamma fields. *Radiat. Meas.* 45(3–6), 594–598. https://doi.org/10.1016/j.radmeas.2010.01.037

Sykora, G.J., Akselrod, M.S., 2010c. Spatial frequency analysis of fluorescent nuclear track detectors irradiated in mixed neutron-photon fields. *Radiat. Meas.* 45(10), 1197–1200. https://doi.org/10.1016/j.radmeas.2010.08.022

Wang, G., Fu, K., Yao, C.S., Su, D., Zhang, G.G., Wang, J.Y., Lu, M., 2012. GaN-based PIN alpha particle detectors. *Nucl. Instr. Methods Phys. Res. A* 663(1), 10–13. https://doi.org/10.1016/j.nima.2011.09.003

Wertheim, D., Gillmore, G., Brown, L., Petford, N., 2010. A new method of imaging particle tracks in solid state nuclear track detectors. *J. Microsc.* 237(1), 1–6. https://doi.org/10.1111/j.1365-2818.2009.03314.x

Yukihara, E.G., Doull, B., Ahmed, M., Brons, S., Tessonnier, T., Jäkel, O., Greilich, S., 2015. Time-resolved optically stimulated luminescence of Al2O3:C for ion beam therapy dosimetry. *Phys. Med. Biol.* 60(17), 6613–6638. https://doi.org/10.1088/0031-9155/60/17/6613